

A survey of the cold molecular gas in gravitationally lensed star-forming galaxies at $z > 2$

M. Aravena,^{1★} J. S. Spilker,² M. Bethermin,³ M. Bothwell,⁴ S. C. Chapman,⁵
C. de Breuck,³ R. M. Furstenuau,⁶ J. González-López,⁷ T. R. Greve,⁸ K. Litke,²
J. Ma,⁹ M. Malkan,¹⁰ D. P. Marrone,² E. J. Murphy,¹¹ A. Stark,¹² M. Strandet,¹³
J. D. Vieira,⁶ A. Weiss,¹³ N. Welikala,¹⁴ G. F. Wong^{15,16} and J. D. Collier^{15,16}

¹Núcleo de Astronomía, Facultad de Ingeniería, Universidad Diego Portales, Av. Ejército 441, 8370191 Santiago, Chile

²Steward Observatory, University of Arizona, 933 North Cherry Avenue, Tucson, AZ 85721, USA

³European Southern Observatory, Karl Schwarzschild Straße 2, D-85748 Garching, Germany

⁴Cavendish Laboratory, University of Cambridge, JJ Thompson Ave, Cambridge CB3 0HA, UK

⁵Dalhousie University, Halifax, Nova Scotia B3H 3J5, Canada

⁶Department of Astronomy and Department of Physics, University of Illinois, 1002 West Green St, Urbana, IL 61801, USA

⁷Instituto de Astrofísica, Facultad de Física, Pontificia Universidad Católica de Chile, Av. Vicuña Mackenna 4860, Casilla 306, Santiago, Chile

⁸Department of Physics and Astronomy, University College London, Gower Street, London WC1E 6BT, UK

⁹Department of Astronomy, University of Florida, Gainesville, FL 32611, USA

¹⁰Department of Physics and Astronomy, University of California, Los Angeles, CA 90095-1547, USA

¹¹Infrared Processing and Analysis Center, California Institute of Technology, MC 220-6, Pasadena, CA 91125, USA

¹²Harvard-Smithsonian Center for Astrophysics, 60 Garden Street, Cambridge, MA 02138, USA

¹³Max-Planck-Institut für Radioastronomie, Auf dem Hügel 69 D-53121 Bonn, Germany

¹⁴Department of Physics and Astrophysics, Oxford University, Denys Wilkinson Building, Keble Road, Oxford OX1 3RH, UK

¹⁵Western Sydney University, Locked Bag 1797, Penrith, NSW 2751, Australia

¹⁶CSIRO Astronomy & Space Science, Australia Telescope National Facility, PO Box 76, Epping, NSW 2121, Australia

Accepted 2016 February 1. Received 2016 January 31; in original form 2015 November 4

ABSTRACT

Using the Australia Telescope Compact Array, we conducted a survey of CO $J = 1 - 0$ and $J = 2 - 1$ line emission towards strongly lensed high-redshift dusty star-forming galaxies (DSFGs) previously discovered with the South Pole Telescope (SPT). Our sample comprises 17 sources that had CO-based spectroscopic redshifts obtained with the Atacama Large Millimeter/submillimeter Array and the Atacama Pathfinder Experiment. We detect all sources with known redshifts in either CO $J = 1 - 0$ or $J = 2 - 1$. 12 sources are detected in the 7-mm continuum. The derived CO luminosities imply gas masses in the range $(0.5-11) \times 10^{10} M_{\odot}$ and gas depletion time-scales $t_{\text{dep}} < 200$ Myr, using a CO to gas mass conversion factor $\alpha_{\text{CO}} = 0.8 M_{\odot} (\text{K km s}^{-1} \text{ pc}^2)^{-1}$. Combining the CO luminosities and dust masses, along with a fixed gas-to-dust ratio, we derive α_{CO} factors in the range $0.4-1.8 M_{\odot} (\text{K km s}^{-1} \text{ pc}^2)^{-1}$, similar to what is found in other starbursting systems. We find small scatter in α_{CO} values within the sample, even though inherent variations in the spatial distribution of dust and gas in individual cases could bias the dust-based α_{CO} estimates. We find that lensing magnification factors based on the CO linewidth to luminosity relation (μ_{CO}) are highly unreliable, but particularly when $\mu < 5$. Finally, comparison of the gas and dynamical masses suggest that the average molecular gas fraction stays relatively constant at $z = 2-5$ in the SPT DSFG sample.

Key words: galaxies: evolution – galaxies: formation – galaxies: high-redshift – galaxies: starburst – cosmology: observations.

1 INTRODUCTION

Panchromatic deep field observations have shown that the cosmic star formation rate (SFR) density decreases by about an order of

★E-mail: manuel.aravenaa@mail.udp.cl

magnitude from $z \sim 3$ to ~ 0 (e.g. Lilly et al. 1996; Bouwens et al. 2014; Madau & Dickinson 2014). An important contributor to the density of star formation at $z \sim 1-3$ is an abundant population of galaxies with extreme SFRs ranging from 100 to 1000 $M_{\odot} \text{ yr}^{-1}$ and large IR luminosities resulting from the re-processing of UV light by the large amounts of dust present. These galaxies have also been termed dusty star-forming galaxies (DSFGs) or submillimetre galaxies (SMGs), referring to the region of the spectrum in which some of the most luminous examples were initially discovered (e.g. Smail, Ivison & Blain 1997; Hughes et al. 1998; Bertoldi et al. 2000; Borys et al. 2002). Current observational evidence suggests that they are likely progenitors of local massive early-type galaxies, and they appear to trace large galaxy overdensities at high redshift (Brodwin et al. 2008; Daddi et al. 2009; Viero et al. 2009; Aravena et al. 2010; Amblard et al. 2011; Capak et al. 2011; Toft et al. 2014).

The primary reservoir of material in the interstellar medium (ISM) of galaxies is cold molecular gas. Large amounts of gas are necessary to sustain the large SFRs in these objects to build up a massive ($> 10^{10} M_{\odot}$), luminous ($> L^*$) galaxy in < 500 Myr. The main components of the molecular ISM are H_2 and He with a minor fraction of heavier molecules. Given the difficulty to detect H_2 in the ISM, the CO molecule (the second most abundant molecule after H_2) has been commonly used to study the gaseous phase of the ISM in galaxies. In particular, the lowest rotational transition of CO $J = 1 - 0$ represents the best studied tracer of the mass and spatial distribution of H_2 in galaxies (Omont 2007; Carilli & Walter 2013). The CO line emission can also be used to estimate the dynamical mass of the host galaxy, avoiding uncertainties due to differential dust obscuration and possible ionized outflows seen in the optical/near-infrared studies.

CO studies of DSFGs have often focused on the observation of high- J ($J \geq 3$) transitions. However, such CO lines trace regions of enhanced star formation or active galactic nuclei activity where high gas excitation is expected (Greve et al. 2014).

Observations of low- J CO line emission in a few unlensed DSFGs at $z \sim 1-3$ indicate that their gas masses can be $2 \times$ larger and up to $3 \times$ more spatially extended than expected based on $J \geq 3$ CO transitions (e.g. Papadopoulos & Ivison 2002; Greve, Ivison & Papadopoulos 2003; Harris et al. 2010; Ivison et al. 2011; Riechers et al. 2011c). These results are reflected in the measured brightness temperature line ratios between the CO(3–2) and CO(1–0) transitions, $R_{31} = T_{32}/T_{10}$. For local thermodynamic equilibrium (LTE), this ratio is expected to be close to unity; however, variations of the line ratios in individual sources make predictions of the low- J CO transitions unreliable. Most CO(1–0) line measurements in distant galaxies, including DSFGs and relatively quiescent star-forming disc galaxies at high redshift, indicate that R_{31} may be frequently as low as 0.5 with significant source-to-source variations, exemplifying the fact that $J > 2$ CO emission lines may not necessarily trace the whole extent of the molecular gas or their total dynamical masses in most cases (e.g. Dannerbauer et al. 2009; Aravena et al. 2010, 2014; Carilli et al. 2010; Harris et al. 2010; Swinbank et al. 2010; Danielson et al. 2011; Ivison et al. 2011; Thomson et al. 2012; Bothwell et al. 2013; Sharon et al. 2013, 2015; Bolatto et al. 2015; Hodge et al. 2015). Indeed, CO measurements in different samples of DSFGs show a significant dispersion, with a median $R_{31} = 0.52 \pm 0.09$ found by Bothwell et al. (2013) and a mean $R_{31} = 0.86 \pm 0.08$ by Spilker et al. (2014). In the case of luminous high-redshift quasars, the CO emission is found to be in LTE typically out to $J = 5$ and the distribution of CO emission, including low- J CO, is mostly found to be concentrated in the inner kpc of the host galaxy, although there is evidence that in some cases the CO emission can be

aligned with the radio jet axis (e.g. Papadopoulos et al. 2008; Elbaz et al. 2009; Emonts et al. 2014). Thus, measurements of molecular gas masses based on $J \geq 3$ CO transitions become difficult due to the uncertainty in the unknown line ratios.

Since observing low- J CO emission at high redshift is observationally time consuming, current CO studies have focused on the most luminous galaxies or gravitationally lensed objects. Methods have been proposed to measure the gas masses from dust mass determinations based on far-IR and submillimetre continuum observations (Bloemen, Deul & Thaddeus 1990; Israel 1997; Dame, Hartmann & Thaddeus 2001; Leroy et al. 2011; Magdis et al. 2011; Magnelli et al. 2012; Scoville et al. 2014). This could open an important window to study the fainter galaxies as continuum observations typically require less observing time, particularly in the era of the Atacama Large Millimeter/submillimeter Array (ALMA). Ideally, both molecular line and dust observations are required because they can provide independent estimates and together yield tighter constraints on the ISM conditions.

The discovery of a population of rare ($n \sim 0.1 \text{ deg}^{-2}$) and extremely bright ($S_{1.4 \text{ mm}} > 15 \text{ mJy}$) mm-selected galaxies in a deep, multiband survey over $\sim 2500 \text{ deg}^2$ of sky with the South Pole Telescope (SPT; Carlstrom et al. 2011), or in the several hundred square degree far-infrared surveys carried out with the *Herschel Space Observatory* (Pilbratt et al. 2010), allows for detailed studies of the ISM properties of DSFGs out to the highest redshifts (Negrello et al. 2010; Vieira et al. 2010; Mocanu et al. 2013; Wardlow et al. 2013). Follow-up high-resolution 870 μm observations with ALMA of a sample of SPT sources showed these are strongly gravitationally lensed galaxies at high-redshift (Hezaveh et al. 2013; Vieira et al. 2013; Weiß et al. 2013). Similar observations with the Submillimeter Array in a sample of bright *Herschel* and *Planck* sources recently found similar results (Bussmann et al. 2013; Cañameras et al. 2015).

After the discovery of bright millimetre SPT sources in a systematic and unbiased way, a major quest began in order to characterize their properties and understand their nature. Blind CO spectroscopic observations with ALMA enabled the redshift confirmation of 28 SPT DSFGs, including two of the highest redshift DSFGs in the literature (Weiß et al. 2013). This represents an ideal sample to study the conditions of the ISM in distant galaxies, with most of the galaxies in the SPT sample (~ 70 per cent) confirmed at $z > 2$. Thus, all the ALMA detected CO transitions in the 3-mm band are $J \geq 3$ (Weiß et al. 2013). Observations of the low- J CO emission are thus necessary to directly trace their molecular gas content and further investigate the nature of these galaxies.

The SPT DSFGs were shown to have large IR luminosities, being $> 10^{12} L_{\odot}$ for most sources even after correcting for lensing magnification (Spilker et al. in preparation; Hezaveh et al. 2013; Ma et al. 2015, this work). Stellar mass measurements of a few SPT DSFGs indicate that they are located above the predicted sequence of secularly evolving star-forming galaxies at $z \sim 2-3$ in the stellar mass versus SFR plane (e.g. Daddi et al. 2007; Elbaz et al. 2007; Noeske et al. 2007; Pannella et al. 2009; Peng et al. 2010; Karim et al. 2011; Rodighiero et al. 2011). The high specific SFRs implied therefore suggest that SPT DSFGs are living in an active starburst phase, likely triggered by major mergers.

In this paper, we present a systematic survey of the low- J CO line emission ($J = 1-0$ and $2-1$) in a sample of gravitationally lensed SPT DSFGs at $z = 2-6$, conducted with the Australia Telescope Compact Array (ATCA). In Section 2, we present our source sample, the ATCA CO data set, lensing models and dust properties that will be used throughout in this study. In Section 3, we show the results

obtained from the ATCA observations. In Section 4, we derive physical properties of the SPT DSFGs based on the reported CO line observations (magnifications, sizes, masses). In Section 5, we discuss the possible implications of our results. Finally, Section 6 summarizes the main conclusions from this paper. Hereafter, we adopt a standard Λ CDM cosmology with $H_0 = 71 \text{ km s}^{-1} \text{ Mpc}^{-1}$, $\Omega_M = 0.27$ and $\Omega_\Lambda = 0.73$.

2 OBSERVATIONS AND DATA

2.1 Sample sources

Our sample is drawn from the brightest sources discovered at 1.4-mm wavelength in the multiband SPT Sunyaev–Zeldovich survey of the southern sky, for which the spectral indexes from the mm photometry were consistent with DSFGs at high-redshift (for details see Vieira et al. 2010; Mocanu et al. 2013). For a subset of 26 of these sources, follow-up spectroscopic observations covering the full 3-mm band (~ 85 – 115 GHz) were obtained with ALMA in order to derive redshifts based on the CO and [C I] line emission (Weiß et al. 2013). For 18/26 sources, it was possible to derive redshifts based on the identification of two or more emission lines. For 5/26 other sources, only one line was identified, and thus the redshifts were constrained using FIR/submm-based photometric redshifts (see Weiß et al. 2013). In the remaining 3/26 sources, no lines were identified (Weiß et al. 2013).

For three other sources, redshifts were identified using spectroscopic observations covering the full 1-mm band (~ 190 – 310 GHz) with the Z-spec instrument on the Atacama Pathfinder Experiment (APEX) 12-m telescope, and confirmed with optical spectroscopy obtained with the Very Large Telescope (VLT). These three sources share the same selection criteria as the ALMA sample of 26 sources (see Weiß et al. 2013). Observations of the CO(1–0) emission in two of these three objects, SPT-S 233227–5358.5 and SPT-S 053816–5030.8, were studied in detail in Aravena et al. (2013). This makes a total of $18+3=21$ SPT sources with confirmed, unambiguous redshifts obtained from millimetre spectroscopy.

Our survey sample is composed of 17 of the 21 SPT sources with redshifts spectroscopically confirmed from ALMA and APEX/Z-spec observations. In these cases, the sources redshifts allowed us to directly target the low- J CO emission lines with the ATCA 7-mm receivers (30–50 GHz). The remaining four sources lie at redshifts where neither low- J CO lines could be observed ($z = 2.84$ – 3.61). One of these four sources correspond to SPT0551–50, which was previously identified at $z = 2.1$ but has recently been revised as $z = 3.1$ (Strandet et al. in preparation).

A wealth of multiwavelength data have been obtained for this sample of galaxies. These include optical spectroscopy of the lens galaxies with the VLT, Gemini and Magellan telescopes and optical/near-infrared imaging with the *Hubble Space Telescope*; mid-infrared imaging with the *Spitzer* Infrared Array Camera at 3.6 and 4.5 μm ; far-infrared imaging with the Photodetector Array Camera and Spectrometer at 100 and 160 μm , and with the Spectral and Photometric Imaging Receiver at 250, 350 and 500 μm on board of the *Herschel* space observatory. Millimetre and submillimetre bands were obtained with the SPT at 3, 2 and 1.4 mm, and with the Submillimeter APEX Bolometer Camera and the Large Bolometer Camera at 350 and 870 μm . For these, independent flux estimates were also obtained with ALMA at 870 μm and 3 mm (Weiß et al. 2013).

2.2 ATCA CO data

We used ATCA in its H214 hybrid array configuration to observe either the CO(1–0) or the CO(2–1) emission line ($\nu_{\text{rest}} = 115.2712$ and 230.5380 GHz , respectively) in the galaxies in our sample. We used the ATCA 7-mm receivers, which can be tuned in the frequency range 30–50 GHz. This frequency range covers the redshift ranges 1.38–2.84 for CO(1–0) and 3.61–6.68 for CO(2–1). Sources with redshifts in the range $z = 2.84$ – 3.61 could not be observed in either of these low- J CO lines. The H214 array configuration at these observing frequencies leads to typical beam sizes of 5–6 arcsec, and thus preclude spatially resolving our sources. A summary of our observations is shown in Table 1.

The observations were performed as part of projects ID C2744 and C2818 during the periods 2012 October 1–10, 2013 March 21–31 and 2013 April 1–7, and were taken under mostly good weather conditions (atmospheric seeing values 90–400 μm) with five working antennas.

We used the Compact Array Broadband Backend configured in the wide bandwidth mode (Wilson et al. 2011). This leads to a total bandwidth of 2 GHz per correlator window and a spectral resolution of 1 MHz per channel (~ 6 – 10 km s^{-1} per channel for the relevant frequency range). In all sources, one of the windows was tuned to observe the CO line, while the other window was tuned to measure the continuum emission or to target another fainter molecular line when possible. Individual tuning frequencies were estimated using the CO-based redshifts from ALMA and APEX/Z-spec spectroscopy (Weiß et al. 2013). The target positions were obtained from the ALMA 3-mm continuum detections (Weiß et al. 2013).

Gain and pointing calibration were performed every 7–10 min and $\sim 1 \text{ h}$, respectively. The gain/pointing calibrators used are listed in Table 1. The bright sources 0537-441 and 1921-293 were used as bandpass calibrators, and Uranus and 1934-638 were used as amplitude calibrators. We expect the flux calibration to be accurate to within 15 per cent, based on the comparison of the Uranus and 1934-638 fluxes. The software package MIRIAD (Sault, Teuben & Wright 1995) and the Common Astronomy Software Applications (CASA; McMullin et al. 2007) were used for editing, calibration and imaging.

The calibrated visibilities were inverted using the CASA task CLEAN using natural weighting and cleaning in a tight box around the source position, down to a threshold of $\sim 2.0\sigma$, where σ is the rms noise level. The final rms and synthesized beam sizes are listed in Table 1.

2.3 Lensing models

ALMA 870 μm continuum imaging at 0.5 arcsec resolution were used to construct gravitational lens models of these objects of all the DSFGs in this study (Spilker et al. in preparation). Lens modelling was performed in the measured visibilities, allowing us to account for residual calibration uncertainties inherent in interferometric measurements and avoiding biases introduced by correlated noise when inverting visibilities into the image plane. The procedure used to derive the lens models is similar to the one used by Hezaveh et al. (2013). All sources were significantly detected in the ALMA images ($\text{SNR} > 50$), providing excellent constraints to these models. Optical and near-infrared spectroscopy of the foreground lenses will be presented in Rotermund et al. (in preparation). The derived magnifications are listed in Table 3.

The ALMA data presented in Spilker et al. (in preparation) have much higher spatial resolution (0.5 arcsec) and sensitivity compared

Table 1. Observation summary.

Source ^a SPT-S	z^b	Line ^c	Freq. (ν_1, ν_2) ^d (GHz)	Obs. dates ^e	Ph. Cal. ^f	Beam ^g	rms ^h (mJy)
J011308–4617.7	4.2328	CO(2–1)	41.800, 44.200	01, 02-Oct-2012	0104-408	4.7 arcsec \times 3.9 arcsec, 81°	0.37
J012506–4723.7	2.5148	CO(1–0)	32.800, 37.500	03-Oct-2012	0104-408	13.0 arcsec \times 4.5 arcsec, 89°	0.65
J024307–4915.5	5.699	CO(2–1)	34.500, 39.700	04, 07, 08-Oct-2012	0252-549	6.2 arcsec \times 5.1 arcsec, 83°	0.22
J034510–4725.6	4.2958	CO(2–1)	41.500, 43.500	09-Oct-2012	0332-403	6.2 arcsec \times 4.7 arcsec, 14°	0.80
J034640–5204.9	5.6559	CO(2–1)	34.500, 39.700	03, 04, 08, 09-Oct-2012	0332-403	6.7 arcsec \times 4.9 arcsec, 88°	0.35
J041839–4751.8	4.2248	CO(2–1)	41.800, 44.200	01, 02-Oct-2012	0422-380	4.9 arcsec \times 3.8 arcsec, 85°	0.45
J044143–4605.3	4.4771	CO(2–1)	42.100, 43.800	03, 07-Apr-2013	0454-463	5.1 arcsec \times 3.9 arcsec, 87°	0.34
J045247–5018.6	2.0104	CO(1–0)	36.600, 38.300	04, 06-Apr-2013	0454-463	5.7 arcsec \times 4.5 arcsec, 87°	0.27
J045912–5942.4	4.7993	CO(2–1)	37.600, 39.700	05-Oct-2012	0516-621	5.7 arcsec \times 4.7 arcsec, 78°	0.30
J055155–4825.0	2.579	CO(1–0)	31.000, 32.500	04-Apr-2013	0537-441	7.0 arcsec \times 5.4 arcsec, 81°	0.40
J210328–6032.6	4.4357	CO(2–1)	41.400, 42.400	21, 23, 24-Mar-2013	2204-540	5.4 arcsec \times 5.1 arcsec, –81°	0.76
J213242–5802.9	4.7677	CO(2–1)	38.400, 40.200	13, 18, 19, 20-Sep-2013	2052-474	5.5 arcsec \times 4.4 arcsec, 77°	0.33
J213404–5013.2	2.7799	CO(1–0)	31.000, 32.800	01, 02-Apr-2013	2052-474	13.0 arcsec \times 5.4 arcsec, 53°	0.45
J214654–5507.8	4.5672	CO(2–1)	41.400, 42.400	22, 24, 29-Mar-2013	2204-540	5.4 arcsec \times 4.6 arcsec, 89°	0.59
J214720–5035.9	3.7602	CO(2–1)	46.600, 48.400	28, 29, 30-Mar-2013	2204-540	4.6 arcsec \times 3.8 arcsec, 88°	0.86

Notes. ^aSource name.

^bCO-based redshift obtained through millimetre spectroscopy with ALMA and APEX/Z-spec in the case of SPT0551–48.

^cTargeted low- J CO transition.

^dCentral observing frequencies for each of the two 2-GHz correlator windows, ν_1 and ν_2 . One of them is tuned to observe the low- J CO, the other is used to have an extra measurement of continuum and to target a fainter molecular line.

^eObserving dates.

^fPhase calibrator used. In several cases, this coincided with the bandpass calibrator 0537-441.

^gSynthesized beam size and position angle.

^hrms level achieved at the low- J CO frequency in a channel of 50 km s^{–1}.

to that presented by Hezaveh et al. (2013), which used only the data taken in the compact configuration at a resolution of 1.5 arcsec. As such, the lens models from Spilker et al. are of much better quality. This explains the discrepancy between the magnification for SPT0418–47 of ~ 21 derived by Hezaveh et al., and the new value of ~ 32 presented in Spilker et al. (in preparation, see Table 3). Note that in the other two sources with lens models in Hezaveh et al. covered here (SPT0346–52 and SPT0538–50) the derived magnifications are fully consistent.

2.4 IR data and models

The far-infrared and (sub-)millimetre data were used to obtain spectral energy distribution (SED) models of the dust emission in the SPT DSFGs (see Greve et al. 2012; Gullberg et al. 2015). The infrared luminosities (L_{IR}), dust temperatures (T_{d}) and masses (M_{d}) used in this study were derived by fitting a single-component modified blackbody dust model to the data (Strandet et al. in preparation). We adopt a dust absorption coefficient $\kappa = 0.045 \times (\nu_{\text{r}}/250\text{GHz})^\beta$ in units of m² kg^{–1}, with ν_{r} the rest-frame frequency in GHz. We use a fixed emissivity index $\beta = 2.0$, with the opacity equals to unity at $\lambda_0 = 100 \mu\text{m}$. Following Greve et al. (2012), we fit the data only to $\lambda_{\text{rest}} > 50 \mu\text{m}$. Infrared luminosities are obtained by integrating the modelled SED in the range 8–1000 μm rest frame. Our SPT DSFGs have complete coverage from $\lambda_{\text{obs}} = 250$ to 3000 μm (Weiß et al. 2013) allowing us for an accurate determination of the dust properties based on seven photometric data points.

To compare with similar high-redshift galaxy samples, we compiled far-infrared photometry for lensed DSFGs and main-sequence (MS) galaxies with published low- J CO detections (Iverson et al. 2010; Combes et al. 2012; Fu et al. 2012; Harris et al. 2012; Johansson et al. 2012; Magdis et al. 2012; Magnelli et al. 2012; Riechers et al. 2013; Rawle et al. 2014), and derived T_{d} , M_{d} and L_{IR} values using the same procedure as that applied to our SPT sources. These

sources were compiled from the various deep extragalactic *Herschel* surveys, and have accurate and complete photometry from *Herschel* and other (sub)millimetre facilities (see also Gullberg et al. 2015).

3 RESULTS

The obtained CO spectra are shown in Fig. 1. Total integrated maps were obtained by collapsing the data cube along the frequency axis in the relevant range containing the detected CO emission line. Total intensities were then computed by spatially fitting a two-dimensional Gaussian to these integrated maps using the task JMFIT from the Astronomical Image Processing System (Greisen 1990). Since all sources are unresolved at the achieved resolution, the CO spectra shown in Fig. 1 are obtained by measuring the fluxes at the CO peak position of the integrated images. To obtain the CO line central frequency and width, we fit single and double component Gaussian curves to the CO spectrum profiles.

The CO spectra of most sources are consistent with single-peaked Gaussian profiles. However, there are two sources where the profile and significance of the detection is consistent with double-peaked profiles, SPT0113–46 and SPT2103–60. Two other sources, SPT0452–50 and SPT0441–46, also show tentative signs of double-peaked CO profiles, but the evidence for multiple components is small at the depth of these data.

The spectrum of SPT2134–50 is shown averaged over broader channels in Fig. 1. In this case, the significance of the detection is $\sim 5\sigma$. The CO(1–0) line profile was checked against that measured in the CO(3–2) line from the ALMA 3-mm spectroscopy (Weiß et al. 2013); we confirm that the linewidth and strength of the lines are consistent. In particular, the ratio between both CO lines, $R_{31} = L'_{\text{CO}3-2}/L'_{\text{CO}1-0} \sim 1$ is comparable to that observed in other star-forming galaxies at high redshift (e.g. Bothwell et al. 2013).

We computed CO luminosities in units of K km s^{–1} pc² using equation 3 from Solomon et al. (1997). Note that L' line

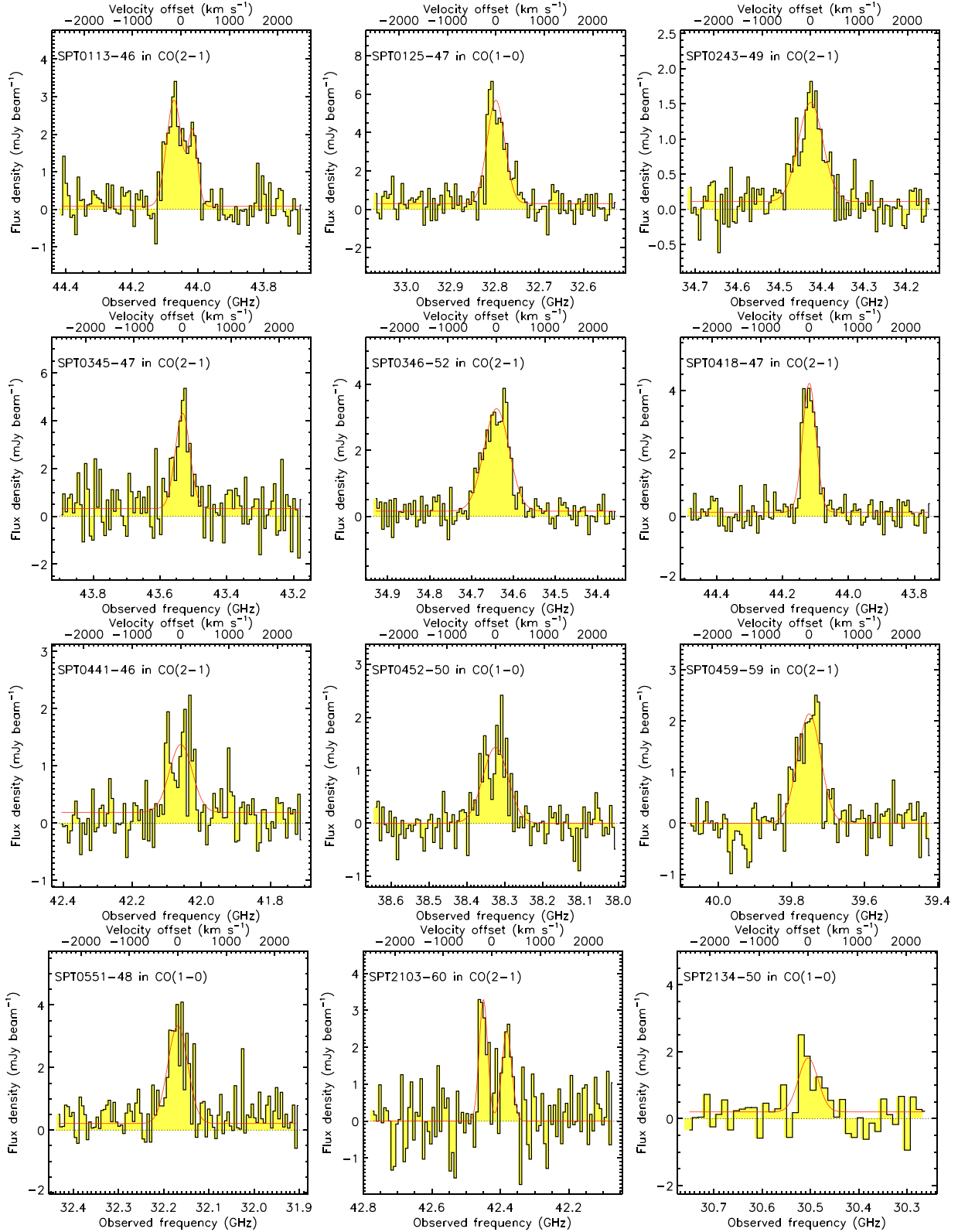


Figure 1. CO (1–0/2–1) emission line spectra obtained with ATCA in our target SPT SMGs. All spectra are shown in 50 km s⁻¹ channels, except for SPT2134-50, which is shown at 120 km s⁻¹ channel resolution. Single or double Gaussian fits are represented by the red lines. The reference for $v = 0$ km s⁻¹ in the upper x-axis has been offset from the inferred ATCA CO redshift.

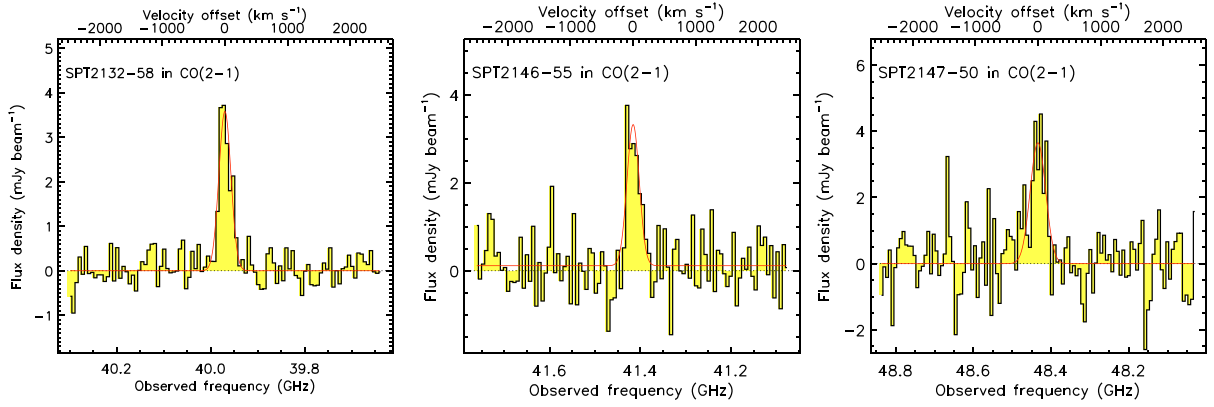


Figure 1 – continued.

Table 2. Observed line and continuum properties.

Source Short name	Transition	z_{CO}^a	v_{FWHM}^b (km s $^{-1}$)	I_{CO}^c (Jy km s $^{-1}$)	L'_{CO}^d (l_0)	S_ν^e (μJy)	ν_{cont} (GHz)
SPT0113–46 ^f	2–1	4.2334(3)	390 ± 42	1.70 ± 0.13	2.63 ± 0.20	125 ± 20	43.0
SPT0125–47	1–0	2.5146(1)	428 ± 27	2.70 ± 0.22	7.93 ± 0.65	230 ± 25	35.2
SPT0243–49	2–1	5.6965(5)	598 ± 47	1.00 ± 0.08	2.43 ± 0.19	120 ± 10	37.1
SPT0345–47	2–1	4.2958(4)	357 ± 55	1.80 ± 0.20	2.85 ± 0.32	170 ± 35	42.5
SPT0346–52	2–1	5.6551(3)	613 ± 30	2.15 ± 0.15	5.16 ± 0.36	160 ± 20	37.1
SPT0418–47	2–1	4.2253(1)	324 ± 19	1.30 ± 0.12	2.00 ± 0.18	145 ± 20	43.0
SPT0441–46	2–1	4.4812(6)	552 ± 77	0.95 ± 0.14	1.60 ± 0.24	130 ± 25	43.0
SPT0452–50	1–0	2.0078(3)	612 ± 59	0.96 ± 0.12	1.91 ± 0.24	<50	37.4
SPT0459–59	2–1	4.7995(4)	561 ± 43	1.10 ± 0.08	2.06 ± 0.32	55 ± 15	38.7
SPT0538–50 ^{f,g}	1–0	2.7855(1)	350 ± 50	1.20 ± 0.20	4.18 ± 0.70	140 ± 20	32.8
SPT0551–48	1–0	2.5833(2)	485 ± 40	1.40 ± 0.20	4.29 ± 0.61	200 ± 50	31.8
SPT2103–60 ^f	2–1	4.4340(3)	476 ± 37	1.60 ± 0.25	2.66 ± 0.41	<135	41.9
SPT2132–58	2–1	4.7678(2)	225 ± 17	0.85 ± 0.07	1.58 ± 0.13	<70	39.3
SPT2134–50	1–0	2.7788(6)	469 ± 180	1.00 ± 0.18	3.48 ± 0.63	140 ± 20	31.9
SPT2146–55	2–1	4.5664(3)	231 ± 37	0.95 ± 0.16	1.65 ± 0.28	<120	41.9
SPT2147–50	2–1	3.7599(4)	290 ± 52	1.25 ± 0.25	1.60 ± 0.32	140 ± 40	47.5
SPT2332–53 ^g	1–0	2.7256(2)	342 ± 42	1.70 ± 0.25	5.77 ± 0.85	<100	33.2

Notes. ^aRedshift from the low- J CO lines.

^bCO line full width half-maximum (FWHM) velocity.

^cIntegrated CO line intensity ($I_{\text{CO}} = \int S_{\text{CO}} d\nu$).

^dObserved CO line luminosity in units of $l_0 = (\times 10^{11} \text{ (K km s}^{-1} \text{ pc}^2)^{-1}$.

^eContinuum flux at the observed frequency ν_{cont} .

^fVelocity difference between the two line peaks is given instead of CO FWHM.

^gObserved properties taken from Aravena et al. (2013).

luminosities are related to L luminosities, in units of L_\odot , by $L/L' = (8\pi k_B/c^2)\nu_{\text{rest}}^3$, where k_B is the Boltzmann constant, c is the speed of light and ν_{rest} is the line rest-frame frequency. For the CO(1–0) line, this yields $L_{\text{CO}}/L'_{\text{CO}} = 4.9 \times 10^{-5}$, with L_{CO} in units of L_\odot . For sources that have been detected in the $J = 2 - 1$ transition, we convert to the ground level by assuming a line brightness temperature ratio between the CO(2–1) and CO(1–0) lines of 0.9. This ratio is consistent with previous findings for DSFGs where an average ratio of 0.85 was found for a sample of 32 sources (Bothwell et al. 2013), consistent within the uncertainties with the line ratio of ~ 0.7 found for star-forming disc galaxies at $z = 1.5$ – 2.0 (Aravena et al. 2010, 2014), and follows the average ratio of ~ 1.1 found through stacking of the SPT DSFGs themselves (Spilker et al. 2014). The measured intensities, luminosities, linewidths and frequencies are given in Table 2.

Measurements of the continuum emission were obtained by collapsing the data along the frequency axis in the line-free SPW and channels around the line. Flux measurements were obtained by fit-

ting a two-dimensional Gaussian to the resulting continuum map. The derived continuum fluxes are listed in Table 2.

4 ANALYSIS

4.1 Linewidths

Previous studies have found a wide range of CO full width at half-maximum (FWHM) linewidths for DSFGs (Neri et al. 2003; Greve et al. 2005; Tacconi et al. 2006, 2008). The mean value for CO FWHM found by Bothwell et al. (2013) in the largest sample of (unlensed) DSFGs studied to date is $510 \pm 80 \text{ km s}^{-1}$. Individual values range from 200–1400 km s^{-1} . Even though this study used mostly $J > 2$ transitions of CO, a subsample of these galaxies were detected in $J = 2$. For these sources, the mean CO FWHM is consistent with the full sample within the statistical uncertainties.

For a more straightforward comparison, in Fig. 2 we show the cumulative distribution of CO FWHM for different samples of galaxies

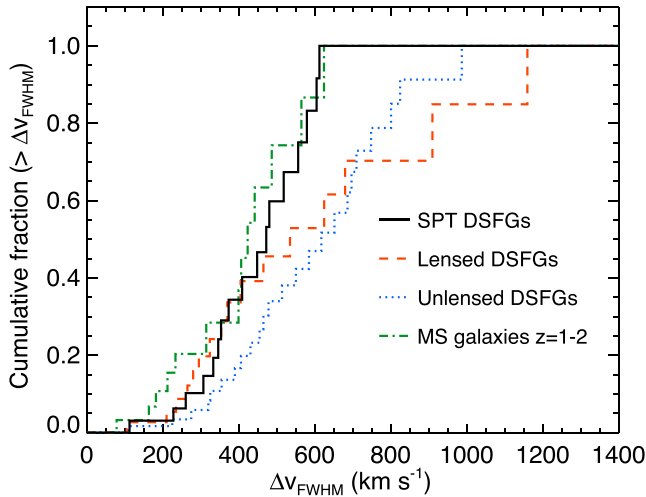


Figure 2. Cumulative distribution of linewidths (FWHM) derived from the CO profiles for the SPT DSFGs, shown as a black solid histogram, compared with the cumulative distribution of linewidths for other high-redshift galaxy samples with available $J \leq 2$ CO measurements. The orange dashed histogram shows the distribution for the lensed DSFGs from literature (see text). The blue dotted histogram shows a literature compilation of unlensed DSFGs and the green dot-dashed histogram represents a sample of MS star-forming galaxies at $z = 1-2$.

that have been detected in low- J CO ($J \leq 2$), including the comparison sample of lensed DSFGs described in Section 2.3 (Ivison et al. 2010; Combes et al. 2012; Fu et al. 2012; Harris et al. 2012; Johansson et al. 2012; Riechers et al. 2013; Rawle et al. 2014), a compilation of 23 unlensed DSFGs from the literature (Coppin et al. 2010; Carilli et al. 2011; Ivison et al. 2011, 2013; Riechers et al. 2011a,c; Thomson et al. 2012; Bothwell et al. 2013; Hodge et al. 2013), and a sample of 13 MS galaxies at $z = 1.0-1.5$ (Daddi et al. 2010; Magnelli et al. 2012).

Qualitatively, the distributions of all samples appear to be different, particularly when comparing with the unlensed DSFG sample. SPT DSFGs have a distribution concentrated at smaller linewidths, whereas most of the unlensed DSFGs from the literature show larger linewidths. Literature lensed DSFGs appear to follow the distribution of SPT DSFGs at linewidths < 400 km s⁻¹, but then they depart to large linewidths. The SPT DSFGs show a weighted-average FWHM of 370 ± 130 km s⁻¹, where the uncertainty includes the scatter in the sample. This compares well with the literature lensed DSFGs, which show a weighted-average FWHM of 320 ± 290 km s⁻¹, and is also compatible with the average for MS galaxies at $z < 2$ of 320 ± 160 km s⁻¹. Unlensed DSFGs, however, show a larger average linewidth of 470 ± 220 km s⁻¹. This difference is obvious from Fig. 2.

To quantify the difference between the linewidth distribution of the various samples, we performed a Kolmogorov–Smirnov (KS) test. We measure the KS probability P that a pair of data sets are drawn from the same distribution. Low values of P indicate that both data sets are significantly different. We compared the FWHM distribution of the SPT DSFG sample with the literature lensed DSFGs, the MS galaxies and the unlensed DSFGs, and found $P = 0.86, 0.60$ and 0.25 , respectively. Such values indicate that the linewidth distribution of the SPT DSFGs is compatible with that of other galaxy populations, in particular, with literature lensed DSFGs (as expected) and MS galaxies. Furthermore, with $P = 0.25$, there is suggestive evidence that the SPT and unlensed DSFG samples do not come from the same linewidth distribution.

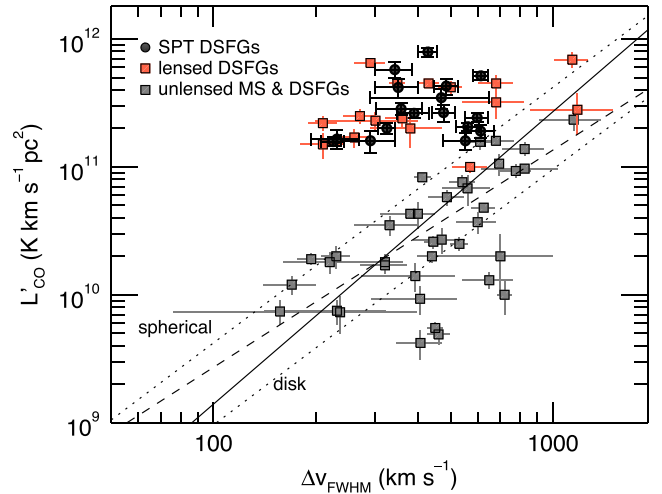


Figure 3. L'_{CO} versus FWHM for our SPT DSFGs (black filled circles), compared to a literature compilation of lensed DSFGs (orange squares) and unlensed DSFGs (grey squares). The solid line shows the best-fitting relation obtained for unlensed DSFGs, which include in this case both SMGs and MS galaxies. The dashed line shows the best-fitting relation found by Harris et al. (2012) for unlensed DSFGs. The dotted lines show a simple ‘virial’ functional form for the CO luminosity for a compact starburst and an extended disc (see text).

4.2 L'_{CO} versus FWHM

Based on physical arguments about the ability of the CO line emission to trace mass and kinematics, Bothwell et al. (2013) suggested an empirical relationship between the CO luminosity (L'_{CO}) and the CO linewidth at FWHM (Δv_{FWHM}), with the form $L' = a(\Delta v_{\text{FWHM}})^b$, where a and b are parameters to be obtained from observational data.

Under the premise that this relationship holds for gravitationally lensed sources, Harris et al. (2012) suggested the use of this relationship to obtain a measurement of the magnification μ , assuming the intrinsic (true) luminosity is related to the observed luminosity by

$$L'_{\text{obs}} = \mu L'_{\text{intrinsic}} = \mu a (\Delta v_{\text{FWHM}})^b. \quad (1)$$

Therefore, $\mu = L'_{\text{obs}} / a (\Delta v_{\text{FWHM}})^b$ can be derived from CO measurements.

In this section, we test the method to obtain lens magnifications from CO, by comparing the true magnification obtained from lens modelling of the dust emission, $\mu_{870 \mu\text{m}}$, for lensed DSFGs with the magnification factors inferred from the CO linewidth– L' relation, μ_{CO} .

Fig. 3 shows the relationship between L'_{CO} and the line FWHM that is obtained for unlensed DSFGs and MS galaxies that have low- J CO detections (Frayer et al. 2008; Coppin et al. 2010; Carilli et al. 2011; Ivison et al. 2011, 2013; Riechers et al. 2011b, 2014; Thomson et al. 2012; Walter et al. 2012; Bothwell et al. 2013; Hodge et al. 2013). We specifically consider only sources with low- J CO measurements (CO 1–0 or CO 2–1) to avoid uncertainties from different line transitions having different linewidths. The solid line shows a best-fitting relationship to unlensed DSFGs and MS galaxies at $z = 1-2$. The dashed line shows the best-fitting relationship presented in equation 2 of Harris et al. (2012), which includes unlensed DSFGs but not MS galaxies. Due to the significant scatter in individual CO luminosities that can span nearly an order of

magnitude and uncertainties in linewidths, both relationships provide a similar fit to the data points.

Following Bothwell et al. (2013), we also show a simple parametrization for L'_{CO} :

$$L'_{\text{CO}} = C \left(\frac{\Delta v_{\text{FWHM}}}{2.35} \right)^2 \frac{R}{\alpha_{\text{CO}} G}, \quad (2)$$

where Δv_{FWHM} is the CO linewidth at FWHM in km s^{-1} , R is the radius of the CO emitting region in parsecs, G is the gravitational constant, α_{CO} is the CO luminosity to gas mass conversion factor in units of $\text{K km s}^{-1} \text{ pc}^2$ and C is a constant that accounts for the geometry of the galaxy (Erb et al. 2006; Bothwell et al. 2013). In Fig. 3, we overlay two cases that bracket the range of L'_{CO} for a given line FWHM: a disc galaxy model for which $C = 2.1$, $R = 5 \text{ kpc}$, $\alpha_{\text{CO}} = 4.6$; and a virialized spherical source geometry with $C = 5$, $R = 2 \text{ kpc}$, $\alpha_{\text{CO}} = 1.0$.

Also shown in Fig. 3 are the CO measurements obtained for the SPT DSFGs and a compilation of gravitationally lensed DSFGs with low- J CO measurements (Ivison et al. 2010; Swinbank et al. 2010; Lestrade et al. 2011; Fu et al. 2012; Harris et al. 2012). The most notable feature is the relatively flat distribution of L'_{CO} values with varying linewidths. This flat distribution suggests that galaxies with narrower linewidths need larger magnification corrections.

To obtain the magnification factor, one only needs to correct by the difference between the observed CO luminosity, and the unlensed L'_{CO} -FWHM relation for a given Δv_{FWHM} . We used our

best-fitting L'_{CO} -FWHM relationship from Fig. 3 to compute a CO-based magnification estimate μ_{CO} for the SPT DSFGs. The derived values are listed in Table 3.

In Fig. 4 we quantify the accuracy of the μ_{CO} values, by comparing them to the magnification values obtained through lens modelling of the dust continuum emission μ_{d} where available (Swinbank et al. 2010; Lestrade et al. 2011; Fu et al. 2012; Busmann et al. 2013; Hezaveh et al. 2013; ; Spilker et al. in preparation).

The large scatter in the unlensed L'_{CO} -FWHM relationship shown in Fig. 3 (about an order of magnitude) makes it highly unreliable to derive accurate magnification factors from CO measurements. For only nine out of the 28 objects with available μ_{d} values (32 per cent of the sample), the difference amounts to $\lesssim 50$ per cent (i.e. $\Delta\mu/\mu < 0.5$ or $0.5\mu_{\text{d}} < \mu_{\text{CO}} < 1.5\mu_{\text{d}}$). This means that most sources have CO-derived magnification values that significantly differ from the values obtained from lens modelling. Interestingly, for several of the sources with $\mu_{\text{d}} < 8$ the CO-based estimate severely overpredicts the magnification ($\Delta\mu/\mu > 1$). Even if we remove the outlier objects (with $\Delta\mu/\mu > 1$), there will be 11 objects with $\Delta\mu/\mu > 0.5$ and only nine objects with $\Delta\mu/\mu < 0.5$.

The reason why the outlier sources show significant deviations with respect to μ_{d} value is not clear, and there is no clear trend among the CO observables (e.g. L'_{CO} , FWHM, signal to noise ratio) that could hint for an effective prior selection of outliers. We suggest two possible explanations for this exceedingly large discrepancies on the derived magnification factor: (1) inaccurate lensing models; and (2) unsampled parameter space in the L_{CO} versus FWHM plane for both lensed and unlensed sources.

Table 3. Derived physical properties.

Source ^a	μ_{870}^b	μ_{CO}^c	T_{d}^d	M_{d}^d	L_{IR}^d	M_{gas}/μ^e	M_{dyn}^f	α_{CO}^g	$\alpha_{\text{CO, lim}}^h$
Short name			(K)	($10^9 M_{\odot}$)	($10^{13} L_{\odot}$)	($10^{10} M_{\odot}$)	($10^{10} M_{\odot}$)	α_0	α_0
SPT0113–46	23.9 ± 0.5	9 ± 2	33 ± 1	3.7 ± 1.0	3.0 ± 0.5	0.9 ± 0.1	2.2 ± 0.5	1.2 ± 0.4	7.0
SPT0125–47	5.5 ± 0.1	21 ± 4	42 ± 2	5.6 ± 1.3	12.3 ± 1.6	11.5 ± 1.0	–	0.7 ± 0.2	0.7
SPT0243–49	5.1 ± 0.2	3 ± 1	35 ± 1	3.4 ± 1.1	4.5 ± 0.8	4.2 ± 0.4	9.8 ± 1.6	1.3 ± 0.4	3.8
SPT0345–47	8.0 ± 0.5	11 ± 4	56 ± 3	1.7 ± 0.4	13.0 ± 2.4	3.2 ± 0.4	2.0 ± 0.6	0.5 ± 0.2	1.8
SPT0346–52	5.6 ± 0.1	6 ± 1	55 ± 2	2.0 ± 0.6	16.2 ± 2.4	8.2 ± 0.6	6.3 ± 0.6	0.4 ± 0.1	2.1
SPT0418–47	32.7 ± 3.0	10 ± 2	49 ± 2	2.5 ± 0.7	7.7 ± 1.3	0.5 ± 0.1	1.9 ± 0.3	1.1 ± 0.3	8.7
SPT0441–46	12.7 ± 1.0	2 ± 1	41 ± 2	2.4 ± 0.7	4.8 ± 0.9	1.1 ± 0.2	4.3 ± 1.2	1.3 ± 0.4	12.3
SPT0452–50	1.7 ± 0.1	2 ± 1	23 ± 1	3.4 ± 0.8	0.7 ± 0.1	9.0 ± 1.2	23.4 ± 4.7	1.8 ± 0.5	1.9
SPT0459–59	3.6 ± 0.3	3 ± 1	41 ± 2	1.8 ± 0.5	4.0 ± 0.8	5.1 ± 0.6	21.9 ± 3.9	0.8 ± 0.2	2.8
SPT0538–50	20.1 ± 1.8	17 ± 6	39 ± 1	5.1 ± 1.2	8.0 ± 1.0	1.7 ± 0.3	4.5 ± 1.3	1.2 ± 0.3	3.3
SPT0551–48	–	8 ± 2	42 ± 2	5.4 ± 1.2	11.0 ± 1.6	3.4 ± 1.8	–	1.3 ± 0.3	3.1
SPT2103–60	27.8 ± 1.8	5 ± 1	40 ± 1	2.5 ± 0.7	4.4 ± 0.7	0.9 ± 0.1	3.1 ± 0.5	0.8 ± 0.3	12.0
SPT2132–58	5.7 ± 0.5	18 ± 4	41 ± 2	1.7 ± 0.5	4.2 ± 0.7	2.5 ± 0.3	0.9 ± 0.2	0.9 ± 0.3	0.9
SPT2134–50	21.0 ± 2.4	7 ± 6	43 ± 2	3.7 ± 0.9	7.2 ± 1.0	1.3 ± 0.3	1.6 ± 1.2	1.1 ± 0.3	7.5
SPT2146–55	6.7 ± 0.4	18 ± 7	49 ± 2	1.7 ± 0.5	3.6 ± 0.8	2.2 ± 0.4	1.3 ± 0.4	0.9 ± 0.3	1.1
SPT2147–50	6.6 ± 0.4	10 ± 5	42 ± 2	1.9 ± 0.5	4.1 ± 0.6	2.2 ± 0.5	2.5 ± 1.6	1.1 ± 0.3	1.7
SPT2332–53	–	25 ± 8	49 ± 2	5.3 ± 1.2	12.2 ± 1.6	4.6 ± 2.4	–	0.9 ± 0.3	1.1

Notes. ^aSource name.

^bMagnification factor obtained through visibility-based lens modelling of ALMA 870 μm continuum imaging data at 0.5 arcsec resolution (Spilker et al. in preparation; Hezaveh et al. 2013).

^cCO-derived magnification factor, computed using the following relation: $\mu_{\text{CO}} = 3 \times (L'_{\text{CO}}/10^{11})(\Delta v_{\text{FWHM}}/400)^{-2.3}$, where L'_{CO} is the measured CO luminosity in units of ($\text{K km s}^{-1} \text{ pc}^2$) and Δv_{FWHM} is the measured linewidth at FWHM in km s^{-1} . See Section 4.2.

^dDust properties derived from multiwavelength SED fitting. The parameters listed here have not been corrected for lensing magnification.

^eGas mass derived from the observed CO luminosity assuming $\alpha_{\text{CO}} = 0.8$, and divided by the lensing magnification μ where available. A typical value of $\mu = 10 \pm 5$ was used when a lensing model was not available, for SPT0551–48 and SPT2332–53.

^fDynamical mass estimated from the line FWHM and the lensing derived effective radius (Spilker et al. in preparation), and assuming a virialized spherical geometry as described in the text. No estimate is provided for SPT0125–47 given the complex source geometry seen in the source-plane ALMA 870 μm image.

^gDust-derived CO luminosity to gas mass conversion factor, in units $\alpha_0 = M_{\odot} (\text{K km s}^{-1} \text{ pc}^2)$.

^hLimit to the CO luminosity to gas mass conversion factor based on a maximum dynamical mass.

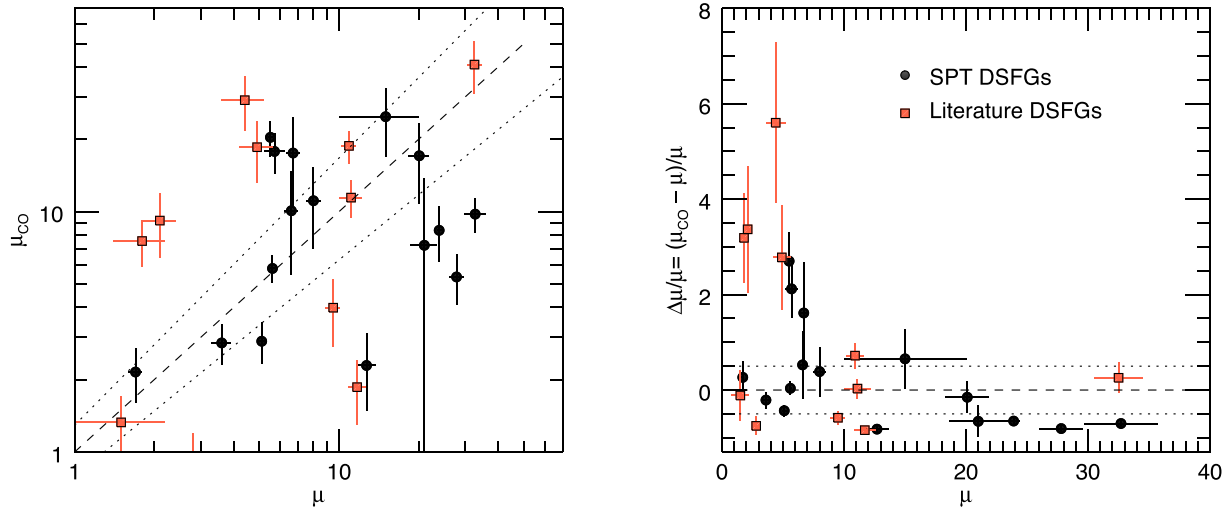


Figure 4. Lensing magnification factors obtained by assuming the best-fitting L'_{CO} versus FWHM line, μ_{CO} , compared to the actual magnification obtained from lens modelling for SPT DSFGs (Spilker et al. in preparation). Also shown are lensed DSFGs from the literature for which a value of μ was available (Fu et al. 2012; Johansson et al. 2012; Bussmann et al. 2013; Riechers et al. 2013). Left: μ versus μ_{CO} . Right: fractional difference between μ and μ_{CO} . The dashed line represents the case where $\mu_{\text{CO}} = \mu$. The dotted lines enclose cases where there is an agreement between both estimates of <50 per cent.

First, this discrepancy might be related to inaccurate lensing models. Four of the sources with the larger μ deviations, which belong to the sample of Harris et al. (2012), do have somewhat peculiar lens configurations as shown by recent high-resolution submillimetre 880 μm imaging (Bussmann et al. 2013). More specifically (see Bussmann et al. for details): J090302.9–014127 presents one of the most compact lens image separations of their sample, and it is possible that the lens itself contributes to the submillimetre emission; J091305.0–005343 corresponds to the largest background source in their sample; In J133649.9+291801, the optical images do not show a lens source, even though the submillimetre map shows evidence for strong lensing; and J141351.9–000026 shows no counter image in the submillimetre map being thus possibly not strongly lensed. Similarly, SPT2132–58 appears to be a compact source in the ALMA images and lens models (Spilker et al. in preparation). Hence, it is possible that the largest differences between the lens-model and CO-based magnification estimates for low μ_{d} are due to a combination of effects, including an inaccurate lens-model for a complex lens configuration and/or due to differential lensing of more compact regions in the submillimetre continuum compared to those more extended seen in CO.

Secondly, the discrepancy in magnification factors could be related to a poorly sampled parameter space in the L'_{CO} -FWHM plane for both lensed and unlensed sources. The measured L'_{CO} for lensed objects is limited to the depth of such observations. Deeper observations of currently CO undetected objects, might extend the range and scatter of L'_{CO} for lensed objects. Similarly, the current low- J CO observations of unlensed objects might not cover the full range of L'_{CO} versus FWHM, particularly for small linewidths ($<500 \text{ km s}^{-1}$) with significant CO luminosities (few $10^{10} \text{ K km s}^{-1} \text{ pc}^2$). In such cases, the current implementation of this L'_{CO} -FWHM method may be flawed and thus would lead to large discrepancies for low μ_{d} .

In summary, our results show that even a rough estimation of the lensing magnification based on unresolved CO measurements is highly unreliable. The large scatter in the L'_{CO} -FWHM relation (driven by the different source geometries), implies that such estimates will be typically off by factors of ~ 2 , particularly when there is independent evidence that the lens configuration could be unusual.

4.3 CO and dust sizes

Assuming that the CO line emission is optically thick, it is possible to estimate the CO emitting size, r_{CO} , even if our observations are unresolved. From the derivation of equation 2 in Solomon & Vanden Bout (2005), and assuming the CO lines have single Gaussian profiles, we find $L'_{\text{CO}} \approx 1.13 \mu (T_{\text{ex}} - T_{\text{CMB}}) \Delta v_{\text{FWHM}} r_{\text{CO}}^2$, where L'_{CO} is the line luminosity in units of $\text{K km s}^{-1} \text{ pc}^2$, μ is the lensing magnification factor, T_{ex} is the gas excitation temperature, in Kelvin, that we assume to be mean dust temperature within the SPT sample, $\sim 40 \text{ K}$, $T_{\text{CMB}} = 2.73(1+z)$ is the cosmic microwave background (CMB) temperature at redshift z , Δv_{FWHM} is the linewidth at FWHM measured in km s^{-1} and r_{CO} is the size of the CO emitting region in parsecs. This expression allows us to estimate the magnification if there is a good CO size measurement. Note also that the expression for r_{CO} depends weakly on the assumed value of T_{ex} , and thus a change of a factor of 2 of this parameter will yield a $\sqrt{2}$ variation on the CO size.

In Fig. 5, we compare the CO size estimated using the above relation with the source sizes derived from the lens reconstruction of the dust emission using the ALMA 870 μm continuum maps, where the latter were available (Spilker et al. in preparation). The CO sizes appear to be up to $2 \times$ larger for most sources; however, four objects appear to have CO sizes smaller than the dust sizes. This is similar to what is observed in the literature (e.g. see detailed discussion by Spilker et al. 2015).

A possible reason for these discrepancies is that galaxies can be morphologically different at different wavelengths and thus the lensing magnification factors for CO and dust could differ significantly, by up to ~ 50 per cent (Spilker et al. 2015). Similarly, differences in the beam filling factors for CO and dust emission may lead to differences in the sizes derived, particularly for our CO size estimate, which does not resolve the source. Note also that a smaller filling factor at fixed flux will not change the CO size estimate, which is based on the flux measurement, and the assumption of $T_{\text{ex}} = T_{\text{d}}$ and optically thick CO, but will increase dust size estimate, which reflects an angular size that will increase as filling factor gets smaller. However, resolved CO imaging of the SPT DSFGs is needed to infer more quantitative conclusions, particularly since

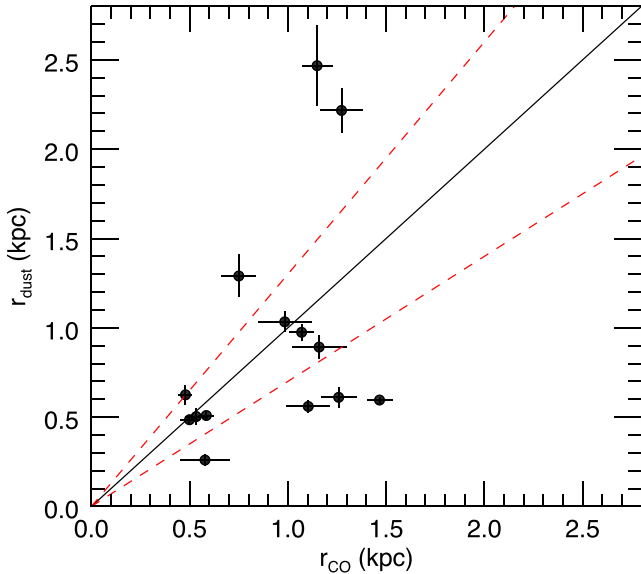


Figure 5. Comparison of the CO and dust sizes for the SPT DSFGs (see Section 4.3). The red dashed lines enclose the location where both estimates differ by less than 30 per cent (i.e. CO sizes are 0.7 and 1.3 times larger than the dust sizes).

the CO size estimation assumes that the dust-derived magnification applies for CO (i.e. assumes no differential lensing) and that the CO linewidth can be approximated as a single Gaussian. The ALMA dust continuum maps provide the more accurate information about the source sizes currently available. Hence, we do not use the CO sizes in the following sections and only use the ALMA-derived dust sizes throughout.

4.4 Dynamical masses

The CO line profiles obtained for our sources allow us to estimate the dynamical mass contained within the CO emitting region. Unfortunately, our CO observations do not resolve the sources spatially, and therefore we do not have information about their resolved CO kinematics. However, the reconstruction of the ALMA 870 μm maps allow us to constrain the size and geometry of the dust emission (we do not use the CO sizes derived above). Our lens reconstruction indicates compact sources, with typical effective radii $< 2\text{ kpc}$ (Fig. 5) and evidence of double component sources in a few cases (Spilker et al. in preparation).

For simplicity, we estimate the dynamical masses of the SPT DSFGs from equation 10 in Bothwell et al. (2013), assuming that the gas is distributed in a virialized spherical system, e.g. a compact starburst. This avoids prior knowledge of the source orientation needed for the computation of the dynamical mass in a disc geometry. We also assume that their molecular gas and dust have the same distribution and extension, and thus the source radius is derived from lens modelling. Using the dust sizes derived from lens models constitute the best assumption in our case with the current data in hand.

The virialized spherical geometry dynamical mass estimator will yield a mass $4.4 \times$ larger than the one obtained by assuming a disc-like gas distribution for the same source size, CO linewidth and an average inclination parameter. However, for a disc-like molecular gas distribution, it would be more reasonable to assume a larger R ($\sim 5\text{ kpc}$ as found by Ivison et al.), yielding a dynamical mass estimate which is similar to the one obtained for a compact gas dis-

tribution. The obtained dynamical masses, for a virialized compact gas distribution, are listed in Table 3.

4.5 Gas masses

One of the most important applications of low- J CO line flux measurements is that they provide an estimate of the mass of molecular gas in a galaxy. The molecular gas mass can be computed from the CO(1–0) line luminosity using the relation $M_{\text{gas}} = \alpha_{\text{CO}} L'_{\text{CO}}$, where α_{CO} is the gas mass to CO luminosity conversion factor. The actual value of α_{CO} has been found to depend on several parameters of the host galaxies, such as metallicity or environment (see Bolatto, Wolfire & Leroy 2013, and references therein). A significant trend was found where galaxies with lower metallicities show higher α_{CO} values (e.g. Wilson 1995; Boselli, Lequeux & Gavazzi 2002; Leroy et al. 2011; Genzel et al. 2012; Schrubba et al. 2012). A similar dependence is found with morphology, where compact starbursts show $\alpha_{\text{CO}} \sim 0.8\text{ K km s}^{-1}\text{ pc}^2$ (Downes & Solomon 1998), whereas more extended discs, such as the Milky Way, show $4\text{--}5 \times$ higher α_{CO} .

An increasing number of galaxies at high redshift ($z > 1$) have an independent α_{CO} estimate and current values range between 0.5 and 5 (Weiß et al. 2007; Tacconi et al. 2008; Daddi et al. 2010; Ivison et al. 2011, 2013; Magdis et al. 2011, 2012; Swinbank et al. 2011; Fu et al. 2012, 2013; Hodge et al. 2012, 2013; Magnelli et al. 2012; Walter et al. 2012; Deane et al. 2013; Messias et al. 2014; Spilker et al. 2015). Typically, studies of DSFGs have used $\alpha_{\text{CO}} = 0.8\text{ K km s}^{-1}\text{ pc}^2$ as found for local ULIRGs (Downes & Solomon 1998) under the implicit assumption that they resemble compact starbursts at high redshift (Bothwell et al. 2013). However, recent studies have shown that this assumption might not always be correct in individual cases (Hodge et al. 2012). For consistency with other DSFG studies, we adopt $\alpha_{\text{CO}} = 0.8$ to obtain the gas masses listed in Table 3. In Section 5.2, we show that the properties of our sources agree with this assumption. Unless otherwise stated, we use α_{CO} in units $\text{K km s}^{-1}\text{ pc}^2$.

5 DISCUSSION

5.1 Star formation efficiencies and gas depletion

The star formation efficiency (SFE) can be defined as the ratio between the SFR and the molecular gas mass, $\text{SFE} = \text{SFR}/M_{\text{gas}}$ in units yr^{-1} . The inverse of this quantity has been termed the gas depletion time-scale, which corresponds to the amount of time required to exhaust all the reservoir of molecular gas at the current rate of star formation, with ($t_{\text{dep}} = M_{\text{gas}}/\text{SFR}$). Typically, given the lack of knowledge about the α_{CO} factor, and thereby intrinsic uncertainty in the estimation of the gas mass, a proxy indicator to the actual SFE has been defined as $L_{\text{IR}}/L'_{\text{CO}}$ in units $L_{\odot} (\text{K km s}^{-1}\text{ pc}^2)^{-1}$.

Fig. 6 shows the observed IR and CO luminosities for the SPT DSFGs compared to other galaxy samples that have comparable observations of low- J CO lines. The SPT DSFGs show an SFE range of $\sim 100\text{--}500 L_{\odot} (\text{K km s}^{-1}\text{ pc}^2)^{-1}$, which is higher than the range occupied by local spiral galaxies and $z \sim 0.4\text{--}2$ MS galaxies of $\sim 20\text{--}100$ (same units). It is interesting to note from the comparison between L_{IR} and L'_{CO} shown in Fig. 6 (left) that with the exception of one source all SPT DSFGs align with the dotted line, which is representative of higher SFE and consistent with local ULIRGs. Fig. 6 (right) also illustrates this point, and suggests a ‘deficit’ of CO luminosity output with respect to L_{IR} for more luminous

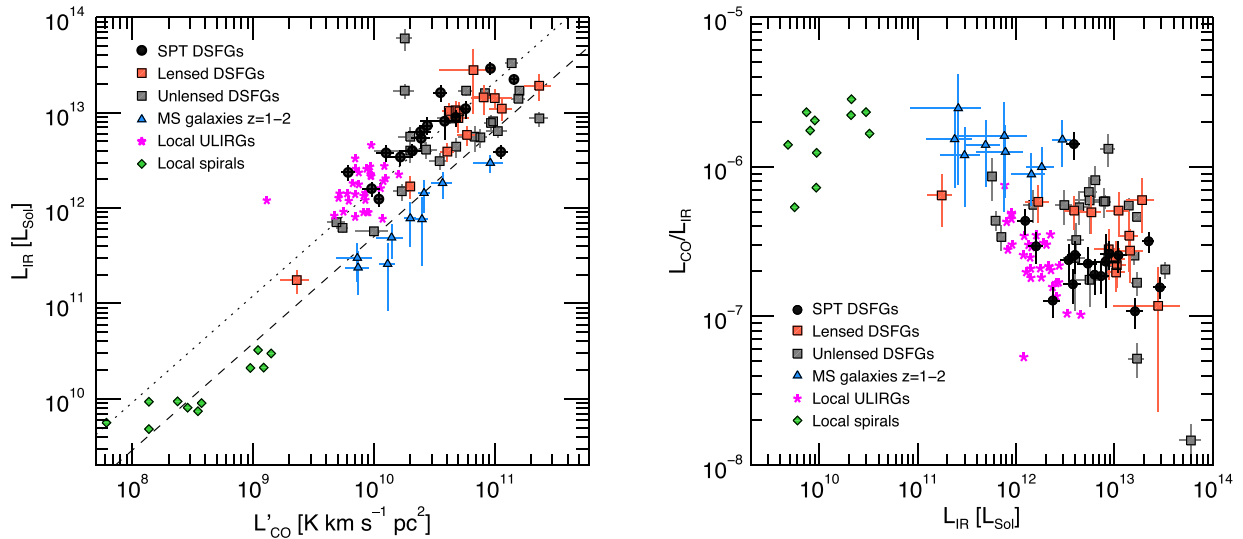


Figure 6. L_{IR} versus L'_{CO} (left) and $L_{\text{CO}}/L_{\text{IR}}$ versus L_{IR} (right) for different galaxy populations that have been detected in low- J CO line emission ($J < 3$). Gravitationally lensed sources are corrected for magnification. The SPT DSFGs are shown as black filled circles. Orange squares show measurements of gravitationally lensed DSFGs that were discovered in various *Herschel* surveys (Harris et al. 2010, 2012; Ivison et al. 2010; Swinbank et al. 2010; Lestrade et al. 2011; Decarli et al. 2012; Fu et al. 2012), while grey squares show unlensed DSFGs (Frayser et al. 2008; Coppin et al. 2010; Carilli et al. 2011; Ivison et al. 2011, 2013; Riechers et al. 2011b,c; Combes et al. 2012; Thomson et al. 2012; Walter et al. 2012; Bothwell et al. 2013; Hodge et al. 2013; De Breuck et al. 2014), respectively. Blue triangles show measurements of massive disc galaxies at $z > 0.4$ (Daddi et al. 2010; Geach et al. 2011; Magnelli et al. 2012). Green squares show measurements of local spiral galaxies (Leroy et al. 2008), and magenta stars represent local ULIRGs (Solomon et al. 1997). Also shown on the left plot are representative fits to local spiral and disc galaxies at high redshift (grey dashed line), $\log_{10} L_{\text{IR}} = 1.12 \log_{10} L'_{\text{CO}} + 0.5$, for guidance. The dotted line shows the same line, with a factor of +0.5 added.

systems (lensed DSFGs are still more luminous than local ULIRGs after magnification correction). While the reason for this is likely that more luminous systems are producing stars at larger rates and therefore consuming the gas fuel faster, it is also possible that in lensed DSFGs the IR emission is being differentially magnified with respect to the cold molecular gas traced by the low- J CO emission, since the IR emission is tracing the *in situ* star-forming regions whereas the CO could be tracing more extended regions within each galaxy. This has been suggested by recent high-resolution CO observations of two SPT DSFGs (Spilker et al. 2015).

Recent observations of MS galaxies have presented evidence for a redshift dependence of the gas depletion time-scale with redshift out to $z = 2$, with the form $\propto (1+z)^{-1}$ (Saintonge et al. 2013; Tacconi et al. 2013; Genzel et al. 2015). These observations are supported by theoretical models that seek to explain the evolution of typical star-forming galaxies using an equilibrium framework, where galaxies have a steady cosmological gas inflow supply that allows them to maintain significant star formation activity over several gigayears. Such models show that the gas depletion time-scales for MS galaxies should evolve as $\propto (1+z)^{-1.5}$ (Dutton, van den Bosch & Dekel 2010; Davé, Finlator & Oppenheimer 2012). With this form, MS galaxies should have roughly constant gas depletion time-scales with redshift, at $z > 3$. Note that recent results found by Genzel et al. (2015), show a weaker dependence of t_{dep} with redshift ($\propto (1+z)^{-0.3}$) for MS galaxies. While this behaviour has been observed in MS galaxies, both lensed and unlensed (Saintonge et al. 2013), it is predicted that galaxies undergoing major mergers should have scattered properties, as they are out of an equilibrium state, and hence should not comply to the aforementioned t_{dep} evolution with redshift.

In Fig. 7, we explore the evolution of the gas depletion time-scale with redshift for the SPT DSFGs compared to other DSFGs from the literature with low- J CO observations. We assume a conversion

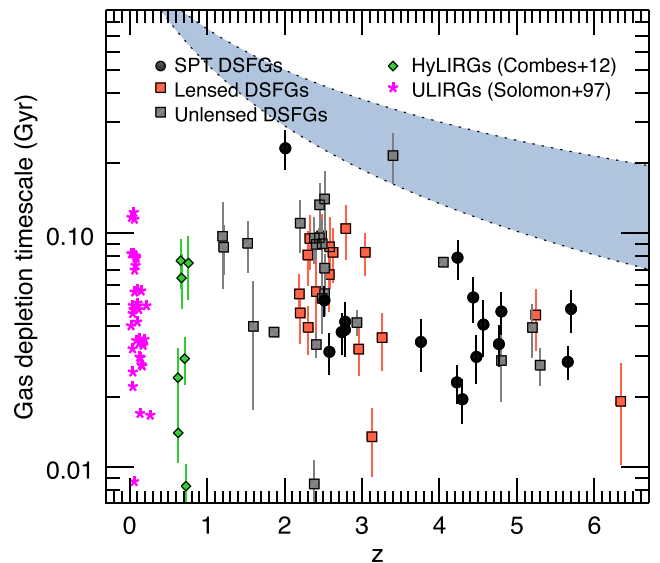


Figure 7. Gas depletion time-scale (t_{dep}) versus redshift (z) for the SPT DSFGs (black circles), compared with other DSFGs from the literature: local ULIRGs (magenta stars; Solomon et al. 1997), HyLIRGs (green diamonds; Combes et al. 2012), unlensed DSFGs (grey squares; Frayer et al. 2008; Coppin et al. 2010; Ivison et al. 2010, 2011, 2013; Carilli et al. 2011; Riechers et al. 2011b, 2014; Thomson et al. 2012; Walter et al. 2012; Bothwell et al. 2013; Hodge et al. 2013; De Breuck et al. 2014) and lensed DSFGs (orange circles; Harris et al. 2010; Ivison et al. 2010; Swinbank et al. 2010; Lestrade et al. 2011; Decarli et al. 2012; Fu et al. 2012; Harris et al. 2012). The shaded regions enclose the curves $1.5 \times (1+z)^{1.0-1.5}$, which is where MS galaxies at $z < 3$ are observed to reside (Saintonge et al. 2013). Measurements for lensed sources assume no differential lensing.

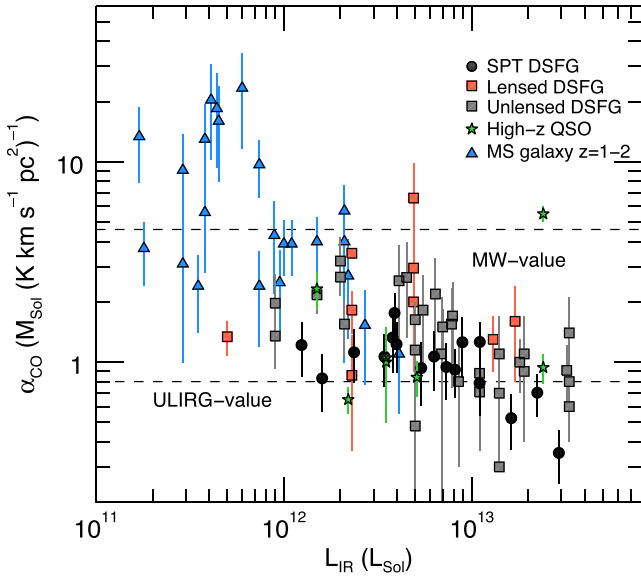


Figure 8. α_{CO} factor versus IR luminosity for SPT SMGs computed from the comparison between the dust-derived $M_{\text{ISM, dust}}$ and L'_{CO} . Also shown are literature compiled values for lensed and unlensed DSFGs, high-redshift quasars and MS galaxies (Weiß et al. 2007; Daddi et al. 2010; Ivison et al. 2011, 2013; Magdis et al. 2011, 2012; Swinbank et al. 2011; Walter et al. 2011, 2012; Fu et al. 2012, 2013; Hodge et al. 2012, 2013; Magnelli et al. 2012; Alaghband-Zadeh et al. 2013; Deane et al. 2013; Messias et al. 2014; Spilker et al. 2015).

between the SFR and IR luminosity of $\text{SFR} = 10^{-10} L_{\text{IR}}$ for a Chabrier initial mass function (Chabrier 2003), and $M_{\text{gas}} = \alpha_{\text{CO}} L'_{\text{CO}}$ and $\alpha_{\text{CO}} = 0.8$. Neither parameter, t_{dep} nor z , depends on the lensing magnification. We assume no differential magnification between the CO and dust emission. We find that the gas depletion time-scales for SPT DSFGs range between ~ 10 – 100 Myr. Furthermore, the data show that the gas depletion time-scales are fairly homogeneous and independent of redshift, suggesting little evolution of this parameter with cosmic time. In all the sources shown in Fig. 7, we are assuming $\alpha_{\text{CO}} = 0.8$. If we were to scale the gas masses to $\alpha_{\text{CO}} = 4.6$, which is not supported by our observations (see below), the data points of the high-redshift objects would lie within the shaded region predicted for MS galaxies, but with a large scatter.

5.2 α_{CO} conversion factor

A different approach to obtain molecular gas masses for galaxies is to use the dust mass as a proxy for the ISM mass content (Leroy et al. 2011; Magdis et al. 2011; Magnelli et al. 2012; Scoville et al. 2014; Genzel et al. 2015). The dust masses can be computed from dust model fits to the IR/submm photometry data. Thereby, under a reasonable assumption of the gas-to-dust ratio (δ_{GDR}), and that the ISM is all molecular, gas masses can be extracted using $M_{\text{gas}} = \delta_{\text{GDR}} M_{\text{dust}}$. The advantage of this approach, for high-redshift samples in particular, is the wealth of IR data available for these samples which allows for the computation of accurate dust models (e.g. from *Herschel* surveys). This method can also be observationally less expensive than measuring CO line fluxes.

By comparing the molecular gas masses derived from dust models with the measured CO luminosities one can provide an estimate of the α_{CO} conversion factor for individual galaxies from $\alpha_{\text{CO}} = M_{\text{gas}}/L'_{\text{CO}}$. In Fig. 8, we show the α_{CO} values for the SPT DSFGs derived using $\delta_{\text{GDR}} = 100$ (Sandstrom et al. 2013), and assuming

no differential magnification between the CO and dust emission. The IR luminosities of the SPT DSFGs have been corrected by lensing magnification by either using the real μ value or assuming the average magnification of the sample, $\mu = 10$, when individual values were not available. For comparison, measurements of α_{CO} in high-redshift galaxies are also shown. These have been computed using a variety of methods including dynamical mass estimates, CO luminosity surface density and gas-to-dust mass ratios. Our results indicate that most SPT DSFGs have values of $\alpha_{\text{CO}} \sim 1$, consistent with other similarly luminous DSFGs and high-redshift QSOs from the literature. Conversely typical $z \sim 2$ MS galaxies show larger values of α_{CO} suggesting a different nature compared to SPT DSFGs. This may also indicate a selection effect, where we have not observed faint enough SPT sources to populate that region of the diagram yet (L_{IR} cutoff).

This method for computing α_{CO} values has important caveats that need to be mentioned. First, this method relies on the simplistic assumption that the dust can be modelled by a single dust temperature. The dust SED may have multiple dust components contributions throughout the galaxy, which are not accounted for in these models. This yields an underestimation of the dust masses and thus our α_{CO} estimates will be biased low. Secondly, if the ISM in these galaxies is highly turbulent, a significant fraction of the gas will have high densities. The α_{CO} factor of such dense gas components will be higher than that from the diffuse emission that dominates the low- J CO lines (Papadopoulos et al. 2012). Thus, the measured α_{CO} from low- J CO observations will be an average of all components, which will not be representative of the high α_{CO} for dense gas (see e.g. Weiß et al. 2007). This is exemplified by the two different determinations of α_{CO} for the quasar host galaxy APM08279+5255. Measurements based on the CO(1–0) line (Weiß et al. 2007), here dominated by dense gas, lead to $\alpha_{\text{CO}} \sim 5.0$ while and [C I] emission line measurements (Walter et al. 2011), related to diffuse regions, yield values closer to ~ 1 (see Fig. 7). These two caveats are applicable to any method aiming to compute the α_{CO} based on low- J CO in DSFGs. Finally, and most importantly, the δ_{GDR} value can vary strongly as a function of metallicity scaling to values up to ~ 1000 (Sandstrom et al. 2013; Rémy-Ruyer et al. 2014). Given the lack of metallicity estimates for our sample, we adopted a fixed value of $\delta_{\text{GDR}} = 100$ for all SPT DSFGs close to the average of $\delta_{\text{GDR}} = 72$ (~ 0.2 dex scatter) determined for a large sample of local star-forming galaxies with solar metallicities (Sandstrom et al. 2013). Since it would not be surprising to find low metallicities in high-redshift galaxies, it is possible that at least a fraction of our sample has high α_{CO} values. Conversely, we should also consider that the increased star formation activity in DSFGs, evidenced by the large intrinsic SFRs, would cause an enrichment of the galaxy’s ISM, lowering the gas content and increasing the metallicity, thereby bringing down the δ_{GDR} and α_{CO} values (Davé et al. 2012).

5.3 The evolution of gas fraction at $z > 2$

If we assume that the star formation is a process that mainly depends on the amount of available gas, then the evolution of the star formation in the Universe is a direct consequence of the evolution of molecular gas supply (Aravena et al. 2012; Bothwell et al. 2013; Walter et al. 2014). Recent studies have shown that there is a strong evolution in the molecular gas fraction with increasing redshift (Tacconi et al. 2010, 2013; Saintonge et al. 2013). Current measurements indicate that MS, normal star-forming galaxies at $z \sim 2$ tend to have larger reservoirs of molecular gas with respect to the bulk amount of baryonic material than they have in the local

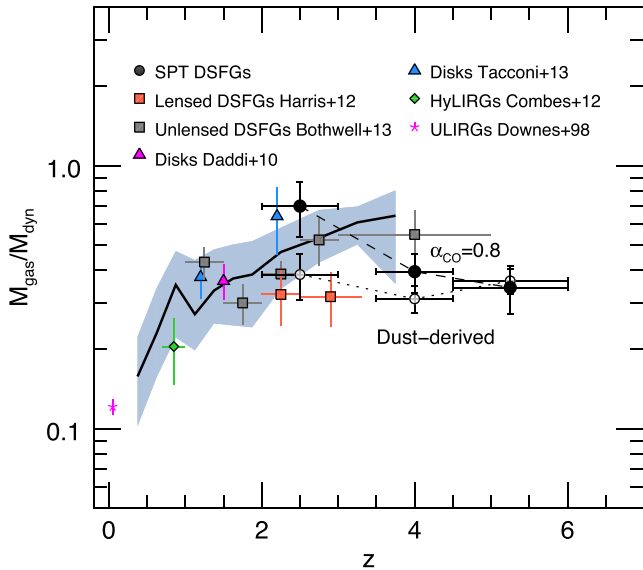


Figure 9. Evolution of gas fractions for DSFGs, computed as $M_{\text{gas}}/M_{\text{dyn}}$. The filled black circles show the gas fraction estimates for SPT DSFGs, where the gas masses were computed from CO luminosities assuming $\alpha_{\text{CO}} = 0.8$. The open circles show the gas fractions for SPT DSFGs, with the gas masses derived from dust models. Also shown are the gas fraction for other galaxy populations: local ULIRGs (magenta star; Downes & Solomon 1998); HyLIRGs (green diamonds; Combes et al. 2012); MS galaxies at $z \sim 1.5$ (magenta; Daddi et al. 2010), and at $z \sim 1.2$ and 2.2 (blue; Tacconi et al. 2013); unlensed DSFGs (grey squares; Bothwell et al. 2013); lensed DSFGs (orange squares; Harris et al. 2012). The grey shaded area shows the average gas fraction for massive star-forming galaxies from models of Béthermin et al. (2015). All gravitationally lensed objects have been corrected for the magnification.

Universe, with the molecular gas fraction defined as $f_{\text{gas}} = M_{\text{gas}}/(M_{\text{stars}} + M_{\text{gas}})$ and M_{stars} as the stellar mass (e.g. Genzel et al. 2015). Using a sample of high-redshift DSFGs, Bothwell et al. (2013) suggested that the molecular gas fraction in galaxies tends to stay constant at $z > 2$, which is well in line with semi-analytic predictions of galaxy formation (Lagos et al. 2011).

In this section, we compute the molecular gas fraction for the SPT DSFGs and compare it with other galaxy populations from the literature. Since we do not have stellar mass measurements for all our sample, we instead compute the molecular gas fraction as $f_{\text{gas}} = M_{\text{gas}}/M_{\text{dyn}}$, where M_{dyn} is the dynamical mass. This assumes that the ISM is molecular dominated.

Fig. 9 shows the molecular gas fraction computed in this way for the SPT DSFGs as a function of redshift. For the SPT DSFGs, the gas fractions are provided using two different estimates of the gas mass, one using the CO luminosities and assuming $\alpha_{\text{CO}} = 0.8$ (shown by filled black circles) and another using the dust masses as explained in the previous section. For comparison, we also show the gas fraction computed in the same manner for other samples in the literature, including ULIRGs (Downes & Solomon 1998), HyLIRGs (Combes et al. 2012), MS galaxies at $z \sim 1-2$ (Daddi et al. 2010; Tacconi et al. 2010, 2013), unlensed DSFGs at $z \sim 1-4$ (Bothwell et al. 2013) and lensed DSFGs at $z \sim 2$ (Harris et al. 2012). For MS galaxies, M_{dyn} was computed assuming a disc like geometry. Where available, M_{dyn} estimates were obtained directly from resolved CO images (Downes & Solomon 1998; Daddi et al. 2010), as they provide more accurate estimates. For HyLIRGs and unlensed DSFGs, dynamical masses were computed using a virialized spherical geometry as explained in Section 4.4, assuming a 1 kpc source radius. For lensed DSFGs, we

only take into account those with measured magnification factors, and compute M_{dyn} using a spherical geometry and a source radius obtained from the lens model (Bussmann et al. 2013, Spilker et al. in preparation).

The shaded area shows the evolution of the average gas fraction ($f_{\text{gas}} = M_{\text{gas}}/M_{\text{dyn}}$) computed by Béthermin et al. (2015). These measurements are based on stacking analysis of the SEDs of a sample of massive star-forming galaxies ($M_{\text{stars}} > 3 \times 10^{10} M_{\odot}$), from which they deduce average dust masses, and thereby converting to gas masses using a local calibration of the metallicity-dependent gas-to-dust ratio (δ_{GDR}). It should be noted that different α_{CO} values have been assumed by the different studies, with $\alpha_{\text{CO}} = 0.8$ for ULIRGs, HyLIRGs and DSFGs, and a Milky Way-like α_{CO} for MS galaxies at high redshift.

Using this metric, Fig. 9 shows an overall decrease in the gas fraction from $z \sim 1$ to 0, particularly seen in HyLIRGs. At higher redshifts, the molecular gas fraction appears to stay almost constant within the uncertainties out to $z \sim 5$. This supports previous findings by Bothwell et al. (2013) and agrees with the overall trend presented by Béthermin et al. out to $z = 3.5$. Similarly, this seems to be in line with the relative homogeneity of the gas depletion time-scales with redshift. However, there is significant scatter in individual M_{dyn} and t_{dep} values, which may be explained by the starbursting nature of the sample and by uncertainties in the M_{dyn} estimates.

SPT DSFGs appear to have average gas fractions of ~ 0.5 , similar to what is found in MS galaxies at $z = 1-2$. The comparison between the gas and dynamical masses can provide constraints on α_{CO} . Assuming $M_{\text{dyn}} > M_{\text{gas}} = \alpha_{\text{CO}} L'_{\text{CO}}$, yields $\alpha_{\text{CO}} < M_{\text{dyn}}/L'_{\text{CO}}$. For the measured CO luminosity and linewidth along with a maximum effective radius from the dust-derived lens models (2 kpc), a limit $\alpha_{\text{CO, lim}}$. Individual limits computed thereby are listed in Table 3. In this computation we are assuming that all the mass is in the form of molecular gas; however, it is still possible that the gas is extended outside the radius defined by dust. This is not possible to quantify without higher resolution CO imaging. Overall, these limits imply that a major fraction of the SPT DSFGs must have low α_{CO} , < 4 , however, it leaves room for up to ~ 30 per cent of the sources to have larger values.

6 CONCLUSIONS

In this paper, we have presented low- J CO observations of a sample of 17 SPT DSFGs that have precise redshift measurements from ALMA CO-based spectroscopy. Our main results are the following.

(i) We detect CO line emission in 17 gravitationally lensed DSFGs from the SPT millimetre survey. The obtained CO luminosities imply molecular gas masses in the range $(1.3-6.3) \times 10^{10} (\alpha_{\text{CO}}/0.8)(\mu/10)^{-1} M_{\odot}$. Comparison with the total IR luminosities indicate short gas depletion time-scales (< 100 Myr) or high SFEs, comparable to that of local ULIRGs.

(ii) Using our CO measurements and accurate lens models for our sample, we quantified the ability to find lensing magnification factors based on the measured CO luminosities and linewidths. We find that this method is highly uncertain, typically finding a magnification μ to within 50 per cent uncertainty, in only 33 per cent of the cases.

(iii) Based on the dust masses computed from multiwavelength SED fitting, we compute gas masses assuming a typical gas-to-dust mass ratio of 100. Comparison of this dust-derived gas mass estimate with the CO luminosities result in low α_{CO} factors for most sources in our sample, with typical $\alpha_{\text{CO}} \sim 1$. Such values

are similar to that found in the most luminous objects ($>10^{12} L_{\odot}$) at high redshift, and are consistent with the values found for local ULIRGs. Several caveats in the computation of this parameter are presented.

(iv) We use the dynamical and gas masses computed from our CO measurements to constrain the average gas fraction ($M_{\text{gas}}/M_{\text{dyn}}$) as a function of redshift. We find that our results are consistent with previous studies of DSFGs that suggest that the gas fraction stays almost constant at $z > 2$.

The CO observations presented in this work support the finding that SPT DSFGs are undergoing an active, short-lived starburst episode. These indicate large reservoirs of molecular gas that is however not enough to sustain the star formation activity for more than a few 100 Myr (the case even if we assume a Milky Way-like α_{CO} factor). This is reflected in Fig. 6, where SPT DSFGs appear located 0.5 dex above the sequence occupied by distant MS galaxies and local, normal spirals (Daddi et al. 2010). Further evidence comes from the derived α_{CO} conversion factor which implies a value of ~ 1 for most individual sources, despite the several caveats on this computation. Besides suggesting a uniformity in the ISM conditions in our sample, it also suggest that the ISM has similar conditions to those found in local ULIRGs, for which a typical value of $\alpha_{\text{CO}} = 0.8$ is found (Downes & Solomon 1998). The final piece of supporting evidence corresponds to the recent results of Spilker et al. (2015). They perform a source–plane reconstruction of the distribution of molecular gas and star formation in two SPT DSFGs, SPT0538–50 and SPT0346–52 at $z = 2.8$ and 5.7 , respectively, both included in the present sample. In the first case, their results suggest a pair of merging galaxies with extended distribution of molecular gas, while in the second case, it shows disturbed dynamics.

Even though the current evidence therefore points towards the conclusion that a dominant fraction of SPT DSFGs are starbursts, we cannot discard the possibility that some SPT DSFGs are driven by cold accretion given the increasing number of DSFGs at high redshift with evident disc-like morphology (Swinbank et al. 2011; Hodge et al. 2012; Carniani et al. 2013; De Breuck et al. 2014).

ACKNOWLEDGEMENTS

MA acknowledges partial support from FONDECYT through grant 1140099. JSS, DPM and JDV acknowledge support from the US National Science Foundation under grant no. AST-1312950. JSS acknowledges support through award SOSPA1-006 from the NRAO. The Australia Telescope is funded by the Commonwealth of Australia for operation as a National Facility managed by CSIRO. The SPT is supported by the National Science Foundation through grant ANT-0638937, with partial support through PHY-1125897, the Kavli Foundation and the Gordon and Betty Moore Foundation.

REFERENCES

Alaghband-Zadeh S. et al., 2013, *MNRAS*, 435, 1493
 Amblard A. et al., 2011, *Nature*, 470, 510
 Aravena M. et al., 2010, *ApJ*, 708, L36
 Aravena M. et al., 2012, *MNRAS*, 426, 258
 Aravena M. et al., 2013, *MNRAS*, 433, 498
 Aravena M. et al., 2014, *MNRAS*, 442, 558
 Bertoldi F. et al., 2000, *A&A*, 360, 92
 Béthermin M. et al., 2015, *A&A*, 573, A113
 Bloemen J. B. G. M., Deul E. R., Thaddeus P., 1990, *A&A*, 233, 437
 Bolatto A. D., Wolfire M., Leroy A. K., 2013, *ARA&A*, 51, 207
 Bolatto A. D. et al., 2015, *ApJ*, 809, 175

Borys C., Chapman S. C., Halpern M., Scott D., 2002, *MNRAS*, 330, L63
 Boselli A., Lequeux J., Gavazzi G., 2002, *Ap&SS*, 281, 127
 Bothwell M. S. et al., 2013, *MNRAS*, 429, 3047
 Bouwens R. J. et al., 2014, *ApJ*, 795, 126
 Brodwin M. et al., 2008, *ApJ*, 687, L65
 Busmann R. S. et al., 2013, *ApJ*, 779, 25
 Cañameras R. et al., 2015, *A&A*, 581, A105
 Capak P. L. et al., 2011, *Nature*, 470, 233
 Carilli C. L., Walter F., 2013, *ARA&A*, 51, 105
 Carilli C. L. et al., 2010, *ApJ*, 714, 1407
 Carilli C. L., Hodge J., Walter F., Riechers D., Daddi E., Dannerbauer H., Morrison G. E., 2011, *ApJ*, 739, L33
 Carlstrom J. E. et al., 2011, *PASP*, 123, 568
 Carniani S. et al., 2013, *A&A*, 559, A29
 Chabrier G., 2003, *PASP*, 115, 763
 Combes F. et al., 2012, *A&A*, 538, L4
 Coppin K. E. K. et al., 2010, *MNRAS*, 407, L103
 Daddi E. et al., 2007, *ApJ*, 670, 156
 Daddi E. et al., 2009, *ApJ*, 694, 1517
 Daddi E. et al., 2010, *ApJ*, 713, 686
 Dame T. M., Hartmann D., Thaddeus P., 2001, *ApJ*, 547, 792
 Danielson A. L. R. et al., 2011, *MNRAS*, 410, 1687
 Dannerbauer H., Daddi E., Riechers D. A., Walter F., Carilli C. L., Dickinson M., Elbaz D., Morrison G. E., 2009, *ApJ*, 698, L178
 Davé R., Finlator K., Oppenheimer B. D., 2012, *MNRAS*, 421, 98
 De Breuck C. et al., 2014, *A&A*, 565, A59
 Deane R. P., Heywood I., Rawlings S., Marshall P. J., 2013, *MNRAS*, 434, 23
 Decarli R. et al., 2012, *ApJ*, 752, 2
 Downes D., Solomon P. M., 1998, *ApJ*, 507, 615
 Dutton A. A., van den Bosch F. C., Dekel A., 2010, *MNRAS*, 405, 1690
 Elbaz D. et al., 2007, *A&A*, 468, 33
 Elbaz D., Jahnke K., Pantin E., Le Borgne D., Letawe G., 2009, *A&A*, 507, 1359
 Emonts B. H. C. et al., 2014, *MNRAS*, 438, 2898
 Erb D. K., Steidel C. C., Shapley A. E., Pettini M., Reddy N. A., Adelberger K. L., 2006, *ApJ*, 646, 107
 Frayer D. T. et al., 2008, *ApJ*, 680, L21
 Fu H. et al., 2012, *ApJ*, 753, 134
 Fu H. et al., 2013, *Nature*, 498, 338
 Geach J. E., Smail I., Moran S. M., MacArthur L. A., Lagos C. d. P., Edge A. C., 2011, *ApJ*, 730, L19
 Genzel R. et al., 2012, *ApJ*, 746, 69
 Genzel R. et al., 2015, *ApJ*, 800, 20
 Greisen E. W., 1990, in Longo G., Sedmak G., eds, *Acquisition, Processing and Archiving of Astronomical Images*. p. 125
 Greve T. R., Ivison R. J., Papadopoulos P. P., 2003, *ApJ*, 599, 839
 Greve T. R. et al., 2005, *MNRAS*, 359, 1165
 Greve T. R. et al., 2012, *ApJ*, 756, 101
 Greve T. R. et al., 2014, *ApJ*, 794, 142
 Gullberg B. et al., 2015, *MNRAS*, 449, 2883
 Harris A. I., Baker A. J., Zonak S. G., Sharon C. E., Genzel R., Rauch K., Watts G., Creager R., 2010, *ApJ*, 723, 1139
 Harris A. I. et al., 2012, *ApJ*, 752, 152
 Hezaveh Y. D. et al., 2013, *ApJ*, 767, 132
 Hodge J. A., Carilli C. L., Walter F., de Blok W. J. G., Riechers D., Daddi E., Lentati L., 2012, *ApJ*, 760, 11
 Hodge J. A., Carilli C. L., Walter F., Daddi E., Riechers D., 2013, *ApJ*, 776, 22
 Hodge J. A., Riechers D., Decarli R., Walter F., Carilli C. L., Daddi E., Dannerbauer H., 2015, *ApJ*, 798, L18
 Hughes D. H. et al., 1998, *Nature*, 394, 241
 Israel F. P., 1997, *A&A*, 317, 65
 Ivison R. J. et al., 2010, *A&A*, 518, L35
 Ivison R. J., Papadopoulos P. P., Smail I., Greve T. R., Thomson A. P., Xilouris E. M., Chapman S. C., 2011, *MNRAS*, 412, 1913
 Ivison R. J. et al., 2013, *ApJ*, 772, 137
 Johansson D. et al., 2012, *A&A*, 543, A62

- Karim A. et al., 2011, *ApJ*, 730, 61
- Lagos C. D. P., Baugh C. M., Lacey C. G., Benson A. J., Kim H.-S., Power C., 2011, *MNRAS*, 418, 1649
- Leroy A. K., Walter F., Brinks E., Bigiel F., de Blok W. J. G., Madore B., Thornley M. D., 2008, *AJ*, 136, 2782
- Leroy A. K. et al., 2011, *ApJ*, 737, 12
- Lestrade J.-F., Carilli C. L., Thanjavur K., Kneib J.-P., Riechers D. A., Bertoldi F., Walter F., Omont A., 2011, *ApJ*, 739, L30
- Lilly S. J., Le Fevre O., Hammer F., Crampton D., 1996, *ApJ*, 460, L1
- Ma J., Gonzalez A. A., SPT SMG collaboration 2015, *ApJ*, 111, 111
- McMullin J. P., Waters B., Schiebel D., Young W., Golap K., 2007, in Shaw R. A., Hill F., Bell D. J., eds, *ASP Conf. Ser. Vol. 376, Astronomical Data Analysis Software and Systems XVI*. Astron. Soc. Pac., San Francisco, p. 127
- Madau P., Dickinson M., 2014, *ARA&A*, 52, 415
- Magdis G. E. et al., 2011, *ApJ*, 740, L15
- Magdis G. E. et al., 2012, *ApJ*, 760, 6
- Magnelli B. et al., 2012, *A&A*, 548, A22
- Messias H. et al., 2014, *A&A*, 568, A92
- Mocanu L. M. et al., 2013, *ApJ*, 779, 61
- Negrello M. et al., 2010, *Science*, 330, 800
- Neri R. et al., 2003, *ApJ*, 597, L113
- Noeske K. G. et al., 2007, *ApJ*, 660, L43
- Omont A., 2007, *Rep. Prog. Phys.*, 70, 1099
- Pannella M. et al., 2009, *ApJ*, 698, L116
- Papadopoulos P. P., Ivison R. J., 2002, *ApJ*, 564, L9
- Papadopoulos P. P., Feain I. J., Wagg J., Wilner D. J., 2008, *ApJ*, 684, 845
- Papadopoulos P. P., van der Werf P., Xilouris E., Isaak K. G., Gao Y., 2012, *ApJ*, 751, 10
- Peng C. Y., Ho L. C., Impey C. D., Rix H.-W., 2010, *AJ*, 139, 2097
- Pilbratt G. L. et al., 2010, *A&A*, 518, L1
- Rawle T. D. et al., 2014, *ApJ*, 783, 59
- R  my-Ruyer A. et al., 2014, *A&A*, 563, A31
- Riechers D. A. et al., 2011a, *ApJ*, 733, L11
- Riechers D. A. et al., 2011b, *ApJ*, 733, L12
- Riechers D. A., Hodge J., Walter F., Carilli C. L., Bertoldi F., 2011c, *ApJ*, 739, L31
- Riechers D. A. et al., 2013, *Nature*, 496, 329
- Riechers D. A. et al., 2014, *ApJ*, 796, 84
- Rodighiero G. et al., 2011, *ApJ*, 739, L40
- Saintonge A. et al., 2013, *ApJ*, 778, 2
- Sandstrom K. M. et al., 2013, *ApJ*, 777, 5
- Sault R. J., Teuben P. J., Wright M. C. H., 1995, in Shaw R. A., Payne H. E., Hayes J. J. E., eds, *ASP Conf. Ser. Vol. 77, Astronomical Data Analysis Software and Systems IV*. Astron. Soc. Pac., San Francisco, p. 433
- Schruba A. et al., 2012, *AJ*, 143, 138
- Scoville N. et al., 2014, *ApJ*, 783, 84
- Sharon C. E., Baker A. J., Harris A. I., Thomson A. P., 2013, *ApJ*, 765, 6
- Sharon C. E., Baker A. J., Harris A. I., Tacconi L. J., Lutz D., Longmore S. N., 2015, *ApJ*, 798, 133
- Smail I., Ivison R. J., Blain A. W., 1997, *ApJ*, 490, L5
- Solomon P. M., Vanden Bout P. A., 2005, *ARA&A*, 43, 677
- Solomon P. M., Downes D., Radford S. J. E., Barrett J. W., 1997, *ApJ*, 478, 144
- Spilker J. S. et al., 2014, *ApJ*, 785, 149
- Spilker J. S. et al., 2015, *ApJ*, 111, 111
- Swinbank A. M. et al., 2010, *Nature*, 464, 733
- Swinbank A. M. et al., 2011, *ApJ*, 742, 11
- Tacconi L. J. et al., 2006, *ApJ*, 640, 228
- Tacconi L. J. et al., 2008, *ApJ*, 680, 246
- Tacconi L. J. et al., 2010, *Nature*, 463, 781
- Tacconi L. J. et al., 2013, *ApJ*, 768, 74
- Thomson A. P. et al., 2012, *MNRAS*, 425, 2203
- Toft S. et al., 2014, *ApJ*, 782, 68
- Vieira J. D. et al., 2010, *ApJ*, 719, 763
- Vieira J. D. et al., 2013, *Nature*, 495, 344
- Viero M. P. et al., 2009, *ApJ*, 707, 1766
- Walter F., Weiß A., Downes D., Decarli R., Henkel C., 2011, *ApJ*, 730, 18
- Walter F. et al., 2012, *Nature*, 486, 233
- Walter F. et al., 2014, *ApJ*, 782, 79
- Wardlow J. L. et al., 2013, *ApJ*, 762, 59
- Weiß A., Downes D., Neri R., Walter F., Henkel C., Wilner D. J., Wagg J., Wiklind T., 2007, *A&A*, 467, 955
- Weiß A. et al., 2013, *ApJ*, 767, 88
- Wilson C. D., 1995, *ApJ*, 448, L97
- Wilson W. E. et al., 2011, *MNRAS*, 416, 832

This paper has been typeset from a \LaTeX file prepared by the author.